# Assessment of Turbulence Models for Transonic / Supersonic Smooth Surface Separation

R. C. Gonzalez, S. A. Prince & D. Di Pasquale
Cranfield University, UK.

*A systematic comparison of the principle modern turbulence prediction methods for the solution of the Navier-Stokes equations for the calculation of high speed flows about slender forebodies at low to moderate angle of attack is presented. This class of flow involves smooth surface turbulent boundary layer separation resulting in steady symmetric leeside vortices, and also the formation of embedded shock waves from the displacement effect of the large vortices in supersonic flow. As such this flow is both complex and highly sensitive to the state of the boundary layers on the body. This study revealed that the method which most consistently provides accurate predictions of the overall forces and moments on the body, the most accurate distribution of surface pressure and can most accurately resolve the flow features, including leeside vortices and embedded shock wave features, is the Solution Adaptive Simulation method. Detached Eddy Simulation and the Reynold Stress Model, which would be expected to provide superior accuracy over the RANS based linear eddy viscosity models, on the whole, failed to provide better predictions. In fact, the k-ε Realizable and k-ω SST turbulence models provided data which was almost as consistently accurate as the Solution Adaptive Simulation method. The standard k-ω turbulence model appears to be completely unsuitable for the computation of this class of high speed flow problem, and this may be associated with the poor initial / default prescription of the value of ω at the far-field boundary.*

## Nomenclature

$C_A$    Axial force coefficient based on afterbody cross-section area.
$C_N$    Normal force coefficient based on afterbody cross-section area
$C_M$    Pitching moment coefficient about the forebody nose, based on afterbody cross-section area.
$D$    Afterbody diameter (m)
$C_p$    Surface pressure coefficient
$L$    Overall length of the body (m)
$M$    Mach number
$p$    Static pressure (Pa)
$P_0$    Total (Stagnation) pressure (Pa)
$P_p$    Pitot pressure (Pa)
$Re_D$    Reynolds number based on $D$.
$x$    Axial distance from the forebody nose (m)
$y, z$    Distance from the forebody nose in the direction of, and at 90º to, the crossflow wind vector respectively.
$\alpha$    Angle of attack (deg)
$\phi$    Circumferential angle around body, from leeward symmetry plane (degrees)
$\infty$    denotes freestream values.

# 1. Introduction

The accurate prediction of the physics of the development of slender body boundary layers, their separation and subsequent formation of leeside vortices is an important prerequisite to the accurate aerodynamic simulation of complete missile and fighter aircraft configurations. The leeside vortical structures generate strong suctions on the body which result in highly non-linear loading characteristics. As these body vortices evolve and convect downstream, they will interact with any aerodynamic surface, intakes or other protuberances which obstruct their path.

As a forebody encounters flow at increasing angle of attack, the leeward flow structure goes through several distinct physical regimes. At incidences above a few degrees the boundary layer on the body will separate as it passes onto the leeside of the body where the local pressure gradient becomes adverse. The separated boundary layer becomes a free shear layer, which possesses a rotational characteristic, or vorticity, due to the higher velocities outward than near the surface. The shear layers then tend to curl up to form well defined vortices in the leeward quadrants. At low to moderate angles of attack these leeside vortices tend to form a symmetric pattern, as illustrated in figure 1, and the flow will be quasi-steady. The fully developed symmetric vortex structure is characterised by strong primary and weaker secondary vortices together with their associated separation and reattachment points. Under certain conditions further, even smaller, vortices may also develop close to the body surface.
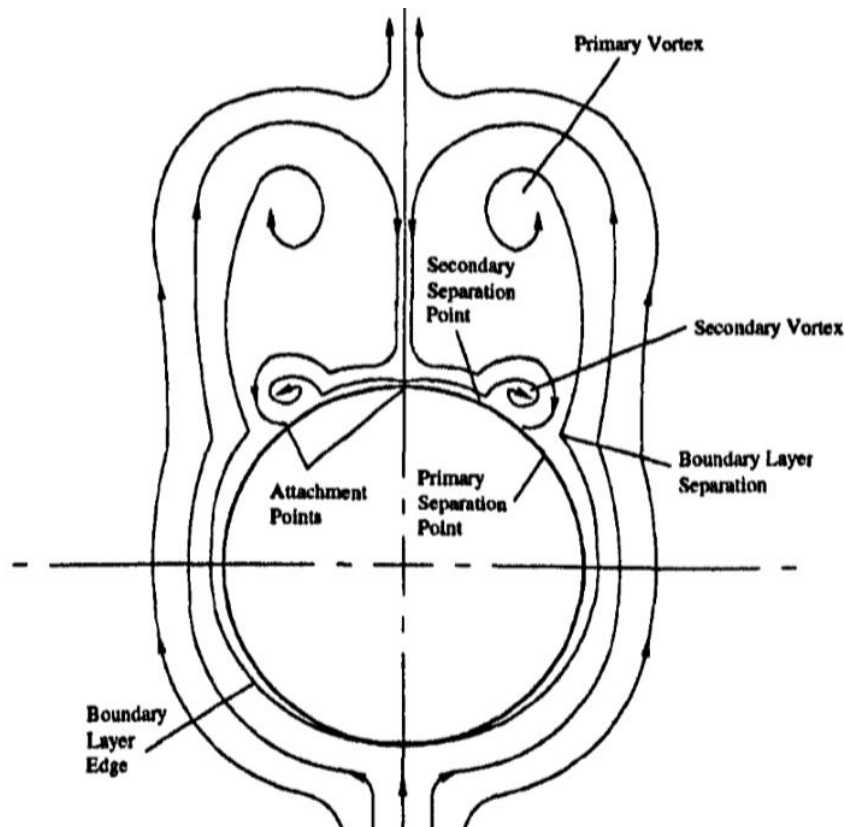


*Figure 1: The crossflow symmetric vortex structure of the moderate a flow around a cylindrical forebody.*

At some critical angle of attack, dependent on the body surface roughness, the flow Reynolds number and external disturbances such as turbulent intensity and acoustic noise, the symmetric pattern breaks down and one vortex will become dominant, located closer to the surface and thereby inducing more suction and therefore a side force. Initially this asymmetric flow regime can exist in a

quasi-steady state. With increased angle of attack, and thereby crossflow pressure gradients, this flow regime then breaks down into one where the flow becomes highly unsteady with vortices successively shed from one side of the body and then the other. In this flow regime, the normal force and side forces generated on the body become unsteady.

The study presented in this report focuses on the prediction of the steady, symmetric vortex flow for moderate angles of attack on smooth surface cylindrical forebodies, and the identification of the most accurate of the turbulence modelling and simulation methods below the fidelity of Large Eddy Simulation. Smooth surface separation of turbulent boundary layers is known to be a significant challenge for modern Navier-Stokes solvers using Reynolds averaging turbulence models, and even for higher fidelity methods which aim to resolve Reynolds stresses or capture, in unsteady simulation, the large eddies in the outer boundary layers. If the windward surface attached boundary layers, and their evolution within high pressure gradients, are not accurately predicted, their separation location and characteristics will also not be properly captured, and the subsequent vortex roll up will result in errors in predicted vortex structure and non-linear force characteristics.

Many investigators have computed such smooth surface slender body flows [1], [2], [3] and have found that the accurate computation of the boundary layer / vortex characteristics is not trivial, especially when the flow field is turbulent. In this study four experimental test cases were chosen, each of which provide detailed and relatively accurate measurements of surface and off-surface flow characteristics, for a comprehensive assessment of the ability of the most commonly employed turbulence models and turbulence simulation methods. A modern high resolution Navier-Stokes solver was employed to model or simulate these four experimental test cases, using seven Reynolds averaging, linear eddy viscosity turbulence models together with the Reynolds Stress Model and two reduced Large Eddy Simulation based methods.

Section 2 of this report details the four experimental tests cases, the flow conditions and measurement methods employed. Section 3 describes the Navier-Stokes solver used and a detailed description of the various turbulence models and simulation approaches used, together with their known advantages and deficiencies. The section also describes the computational meshes used and the strategy employed to ensure grid independent results. The results and comparative analysis for the four test cases investigated are presented in section 4, and the final conclusions derived from the study are presented in section 5.


## 2. The Experimental Test Cases

All four experimental test cases used a classic three calibre tangent-ogival cylindrical cross-section forebody of diameter, $D$, with an extended cylindrical afterbody giving a total body length, $L$. Table 1 presents the details for each of the experimental test cases used in this study, including freestream Mach number, $M_\infty$, angle of attack, $\alpha$, stagnation pressure, $P_0$, stagnation temperature, $T_0$, and Reynolds number based on afterbody diameter, $Re_D$
.

| Case | Body | $D$ (mm) | $L/D$ | $M_\infty$ | $\alpha$ (deg) | $Re_D$ | $P_0$ (kPa) | $T_0$ (K) |
|------|------|----------|-------|------------|----------------|--------|-------------|-----------|
| 1 | B2 | 80 | 15 | 2.0 | 0 | $1.2 \times 10^6$ | 120 | 300 |
| 2 | B2 | 80 | 15 | 2.0 | 10 | $1.2 \times 10^6$ | 120 | 300 |
| 3 | B1A | 93.98 | 13 | 0.7 | 14 | $0.667 \times 10^6$ | 51 | 294 |
| 4 | B1A | 93.98 | 13 | 2.5 | 14 | $1.123 \times 10^6$ | 142 | 308 |

*Table 1: Experimental details for each of the four test cases.*

The first and second test cases were provided by the French Office National d'Études et de Recherches Aérospatiales (ONERA), which tested a 15 calibre body, designated B2, in the in the 0.30m x 0.30m ONERA S5Ch wind tunnel [4]. In these experiments turbulent boundary layers were tripped using transition strips located at $x/D$=0.15. Measurements were made of surface pressures using surface embedded tapping for both test cases. For case 1, at zero incidence, the Mach number and total pressure ratio was measured within the boundary layer at $x/D$ stations of 3, 5, 7, 9 and 12. For case 2, for $\alpha = 10^{\circ}$, surface pressure was measured circumferentially at $x/D$ stations 5, 7 and 9. Crossflow contours of total pressure, Mach number and local flow angle were measured at the same axial stations using a five hole probe and a traverse system. The experimental accuracy was determined from a repeatability assessment. The freestream conditions were quoted with the following accuracy: $\Delta M = \pm0.01$, $\Delta P = \pm30$Pa within the range 2 – 50kPa and $\Delta\alpha = \pm0.1^{\circ}$. The five-hole probe was calibrated with the following quoted accuracy: $\Delta M = \pm0.02$, $\Delta P = \pm30$Pa within the range 2 – 50kPa and $\Delta\alpha = \pm0.2^{\circ}$. The spatial accuracy of the traverse mechanism was quoted as $\Delta x$, $\Delta y$, $\Delta z = \pm0.2$mm. Barberis [5] states that the various properties were measured with an accuracy of 2 – 3% in regions where gradients were moderate, but at 5 – 10% in the core of the more intense vortices where gradients are much higher.

Test cases 3 and 4 come from experiments at the UK Defence Research Agency (formerly the Royal Aerospace Establishment) in Bedford by Ward et al [6], [7], [8]. The model, designated B1A, consisting of a 13 calibre cylindrical body of 3.7 inch diameter having a 3 calibre tangent-ogival nose, was common to both tests. For test case 3, the model was tested in the 8ft x 8ft High Speed Wind Tunnel at a Mach number of M=0.7, and for case 4 at Mach 2.5 in the 3ft x 4ft High Speed Supersonic Tunnel. Both experiments were performed with a transition strip of carborundum grit of height 0.5mm at $x/D$ = 0.3. Surface pressure measurements were acquired using the same technique used in the ONERA B2 tests, while crossflow contours of total pressure ratio (for the transonic case 3) and pitot pressure ratio (for the supersonic case 4) were measured using a traversing pitot-static tube with the same spatial accuracy as that in the ONERA tests. Pitot pressure, $p_p$, is the local total pressure measured by a pitot tube in a supersonic flow where the nose of the tube generates a locally normal detached bow shock wave, thereby reducing the total pressure from its freestream value, and is obtained with the Rayleigh pitot equation:

$$p_p = p \left( \frac{(\gamma + 1)^2 M^2}{4\gamma M^2 - 2(\gamma - 1)} \right)^{\gamma/(\gamma-1)} \frac{1 - \gamma + 2\gamma M^2}{\gamma + 1} \tag{1}$$

where $M$ and $p$ are the local values of the is the Mach number and static pressure respectively. The pitot pressure ratio, $p_p/p_{p\infty}$, is simply the ratio of the local to the freestream value of this pressure. Freestream test conditions for each test are presented in table 1. Experimental accuracy was quoted as: $\Delta C_p = \pm0.003$, $\Delta(P_p/P_{p\infty}) = \pm0.0025$, $\Delta M = \pm0.01$ and $\Delta\alpha = \pm0.05^{\circ}$.

# 3. The Computational Study

## 3.1 Computational Fluid Dynamics

The Navier-Stokes equations are a set of coupled differential equations that predict all physical flow features of an unsteady, compressible, viscous continuum flow. The idea behind Computational Fluid Dynamics relies on the mathematical manipulation of these governing equations to predict the flow properties of a specific case given a set of initial conditions, all this through an iterative process in a computer. This manipulation generally consists of the division of the flow domain into discrete control volumes (cells) and the integration of these governing equations along them through the use of Gauss divergence theorem as part of the Finite Volume Method [9].

Assumptions can be made to produce reduced forms of the Navier-Stokes equations that are generally computationally less expensive. These forms however exist at the expense of accuracy depending on the way they approximate the Navier Stokes equations and model the physical flow features. A graphic comparison of some of these approximation methods is presented in figure 2 by order of complexity and fidelity, starting from the full unsteady solution of the Navier-Stokes equations by Direct Numerical Simulation down to the solution of the incompressible potential-flow equations done in Panel methods, i.e., linearised potential methods.
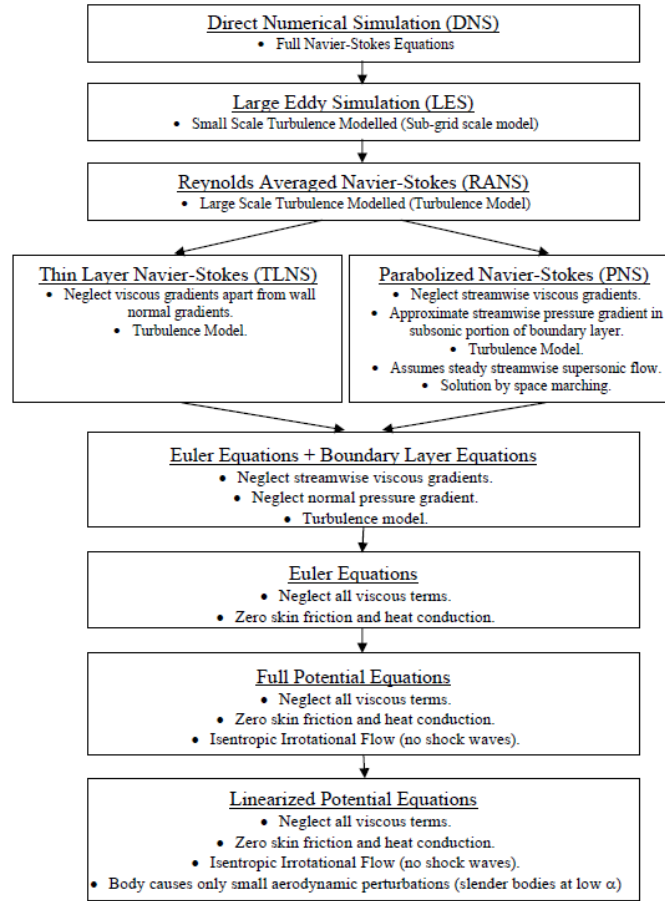


*Figure 2. Approximations of the governing equations for continuum flow. Prince [10]*

The potential methods represent the least accurate way to determine the flow features of a given case. The method assumes inviscid, incompressible, steady and irrotational flow and vortices are only modelled through potential flow. Consequently, they have a minimal range of applicability and are mainly used to provide rough estimates of aerodynamic forces of simple/simplified bodies.

In the models based on the Euler equations, the flow is assumed to be inviscid and adiabatic, and viscous phenomena are not physically described. Solution of the boundary layer equations can be coupled with the Euler method, and boundary layer separation can be modelled by explicit boundary conditions to force flow separation. This method has been shown to be capable of capturing vortical structures in steady, incompressible flow on sharp-edged delta wings with plausible correlations [11], given the essentially inviscid nature of the large scale eddies of a fully developed leading-edge vortex. Regardless of the capabilities of these approximation methods, to adequately study cases where viscosity plays a significant role, such as the formation of secondary and tertiary vortex systems, the vortex breakdown or the vortex core region, more accurate, high-order methods are required.

On the other side of the spectrum, Direct Numerical Simulation (DNS) represents the most comprehensive simulation method currently available. In this case, the unsteady Navier-Stokes equations are solved directly as a function of space and time, resulting in a complete description of a

turbulent flow. The method requires a sufficiently fine mesh and sufficiently small time steps to resolve the smallest turbulent eddies (Kolmogorov length scale) and the fastest velocity fluctuations [12][13]. Consequently, the calculations become so computationally demanding that the application of the method is generally limited to fundamental physics studies, including incompressible flow and Reynolds numbers much lower than those of typical practical applications [13].

The Large Eddy Simulation (LES) method is an intermediate form of turbulence calculation in which a spatial filtering operation is done to separate the large and small scale motions so that the full unsteady Navier-Stokes equations can be solved within regions with length scales greater than a specific cut-off size, while the zones with smaller turbulent scales are modelled with a sub-grid-scale (SGS) model [9]. This method requires a complex algorithm to smoothly blend the resolved scales and the modelled effects, and although it can handle more complex geometries and higher Reynolds numbers than DNS, it is still computationally demanding and is used only sparingly for practical applications [13].

Another approximation method is the Reynolds-Averaged Navier-Stokes (RANS) method and is focused on the mean flow properties. For this method, Reynolds decomposition (i.e., the definition of a property as the sum of a steady mean component and a time-averaged fluctuating one) is applied to the flow velocity components and static pressure before being replaced in the continuity and Navier-Stokes equations, which are then time-averaged and solved through the use of turbulence models. These models consider different approaches to obtain the Reynolds stresses that result from the time averaging operation and express them as a function of eddy viscosity through the Boussinesq assumption, to close the Reynolds-Averaged Navier-Stokes equations and compute the features of turbulent flows.

The RANS approximation is the most widely used for practical applications due to its proven reliability and reasonable computational cost. However, given that it only produces steady solutions to the governing equations, it is not suitable for the study of unsteady phenomena such as the vortex breakdown. Another limitation inherent in eddy viscosity models is the inaccurate assumption of isotropic turbulence (i.e. constant fluctuations in different directions) which further reduces the accuracy of the predicted unsteady phenomena[9][13].

The Unsteady Reynolds-Averaged Navier-Stokes (URANS) approximation attempts to address these limitations by retaining the transient (unsteady) term in the momentum equation while using the classical RANS approximation [14][15]. Unfortunately, preliminary computations on bodies at high angles of attack were equivalent to steady RANS simulations and did not capture any significant unsteadiness [11].

A hybrid RANS/LES approach known as Detached Eddy Simulation (DES) was developed to model the near-wall regions using a RANS approach and to resolve the rest of the flow through the LES approximation. The method leverages some of the features of RANS and LES, which ultimately allow for less computationally demanding unsteady simulations while achieving high levels of accuracy. The more flexible grid size requirements and the isotropic assumption of the RANS approximation allow for the modelling of the smaller eddies found inside the boundary layer (which are nearly isotropic in nature for flows at high Reynolds numbers [14]). On the other hand, the capabilities of LES more properly resolve the flow regions governed by the more anisotropic larger eddies [15].

A modified distance function that depends on the local grid spacing (i.e. the maximum cell length among the three grid directions) and the wall distance, is used to switch from RANS to LES modes. The function works in such a way that the RANS mode operates when the wall distance is smaller than the grid spacing, and the LES mode works outside the boundary layer where the grid spacing is smaller. This method is, however, prone to failure due to its high dependence on grid size. Depending on the case, the use of a mesh of inadequate size, could activate the LES mode inside the boundary layer and result in a poorly resolved region and inaccurate predictions if the mesh is not fine enough for the LES approximation to resolve the small eddies present in this area [15][16]. This switch in method due to ambiguous grid features is known as Modelled-Stress Depletion (MSD) and represents the main limitation of the method.

The Delayed-Detached Eddy Simulation (DDES) approach is a modified version of DES that uses an adjusted switching function to "shield" the boundary layer and delay the LES mode. This function considers boundary layer information such as the kinematic eddy viscosity, the molecular viscosity and velocity gradients to blend it with any eddy viscosity model better and avoid erroneous switches of approximation [16].

Another approach developed to address the MSD phenomena is known as Scale Adaptive Simulation (SAS). The method uses an improved URANS formulation that relies on the use of the von Karman length scale (i.e. a parameter based on the ratio between the first and the second velocity gradients), rather than the explicit grid spacing used in DES or the turbulent length scale used in RANS models, to determine the local scale of the flow field. This allows the SAS models to automatically adjust to the length-scale present in the case and behave in a LES manner in unsteady regions, while using a RANS formulation in stable zones [17][18][19].

To sum up, the selection of an approximation method to the Navier-Stokes equations for the analysis of a given case study requires a deep understanding of its advantages and limitations as well as the nature of the involved phenomena involved. In the context of the present study, the use of inadequate methods could lead to an inaccurate description of the evolution of an attached boundary layer in an adverse pressure gradient and would imply erroneous predictions of: 1) its separation point and roll-up features, and 2) the global effect of the resultant vortices on the body aerodynamic forces. The development of models for the prediction of vortex flows for general aerospace applications represents a still ongoing effort and, in Luckring [11], a detailed chronological review on the progress up to recent years is presented.

Altogether, the present study will focus on the capability assessment of RANS, DDES and SAS approaches, given the improved level of accuracy of the latter methods and the "cost-benefit" advantage of RANS models. The following section will provide in-depth insight of the RANS method, given the amount of currently available turbulence models, and will present details on their respective formulation as well as their capabilities in the framework of the present study.

## 3.2 RANS Turbulence modelling

As previously explained, the Reynolds-Averaged Navier-Stokes equations, result from the Reynolds decomposition applied to the Navier-Stokes equations and the further time-average taken on the resultant expressions. Equation 2 shows the final equation for the x momentum, where $U$ and $u_i$ respectively represent the flow velocity and its x component.

$$\frac{\partial(\overline{\rho u_\iota})}{\delta t} + div(\overline{\rho u_\iota U}) = -\frac{\delta \bar{P}}{\delta x_i} + div\big(\mu \, grad(\bar{u}_\iota)\big) - div(\overline{\rho u'_\iota U'}) \qquad (2)$$

$$(I) \qquad (II) \qquad (III) \qquad (IV) \qquad (V)$$

In this case, the averaging operation introduces six additional terms, known as Reynolds stresses, which involve the interaction of fluctuating velocities and are related to the momentum exchange between turbulent eddies, as shown by term (V) of equation 2. These terms correspond to three normal and three shear stresses and generate the so-called closure problem: a system of four equations (the continuity and Navier-Stokes equations) with ten unknowns (three velocity components, pressure and six Reynolds stresses) [15].

In the RANS method, turbulence models are used to predict the Reynolds stresses and close the system of equations. These models are based on Boussinesq's hypothesis, shown in equation 3, which evolved from the assumption that Reynolds stresses have an analogous nature to the viscous ones and can therefore be described by Newton's law of viscosity.

$$-\overline{\rho u'_i U'} = \mu_t \left( \frac{\delta \bar{u}_i}{\delta x_j} + \frac{\delta \bar{u}_j}{\delta x_i} \right) - \frac{2}{3} \rho k \delta_{ij}$$

$$(I) \qquad\qquad (II) \qquad\qquad (III)$$

(3)

The term (III) of the equation features $k$ which represents the mean turbulent kinetic energy per unit of mass and $\delta_{ij}$ known as Kronecker's delta, which deals with the normal stresses. The equation also features $\mu_t$ in term (II) which is the turbulent or eddy viscosity and represents the unknown part that the so-called linear Eddy Viscosity Models (EVM) aim to predict. In this regard, these models are generally classified based on the number of additional transport equations that need to be solved along with the RANS equations and some of them are outlined below.

### 3.2.1 Zero-equation EVM

In this type of model the turbulent viscosity is obtained algebraically, and for this reason they are also known as Algebraic Eddy Viscosity Models. Amongst them, the Baldwin-Lomax model [20] is also classified as a two-layer model in the sense that it splits the boundary layer into two regions, an inner and an outer, and considers different formulations to treat each one of them. In the inner region, the turbulent viscosity $(\mu_t)_{inner}$ is obtained through the Prandtl-Van Driest formulation, while in the outer, the viscosity $(\mu_t)_{outer}$ is found through a modification of the Cebeci-Smith model [21], as shown by equation 4 [20]. The model uses the local distance normal to the wall as reference and considers the smallest distance at which both inner and outer turbulent viscosities are equal, as the switching parameter between regions, i.e., $y_{crossover}$.

$$\mu_t = \begin{cases} (\mu_t)_{inner} = \rho(kyD)^2|\omega| \,, y \le y_{crossover} \\ (\mu_t)_{outer} = K C_{cp} \rho F_{wake} F_{kleb} \,, y > y_{crossover} \end{cases}$$

(4)

In equation 4, $\rho$, $k$, $D$ and $|\omega|$ in $(\mu_t)_{inner}$ respectively correspond to the density, Karman constant, Van-Driest damping factor and magnitude of vorticity, while $K$ in $(\mu_t)_{outer}$ represents the Clauser constant, $F_{kleb}$ is an intermittency function, $C_{cp}$ is a constant derived from the Cebeci-Smith model formulation [34] and $F_{wake}$, is given in equation 5, and is proportional to both the maximum value of the function $F(y)$ defined in equation 6 and its normal position.

$$F_{wake} = y_{max} F_{max}$$

(5)

$$F(y) = |\omega| y \left[ 1 - e^{-\left( y^+/A^+ \right)} \right]$$

(6)

Where $A^+$ in equation 6 is a constant used in the Van Driest formulation and $y^+$ is the friction height. The values of these constants are given in reference [20].

At its core, the formulation of the model searches outward for the peak in $F(y)$, cuts off once the peak is reached and repeats the analysis at each axial station around the body. The model tends to overestimate $(\mu_t)_{outer}$ in bodies with large crossflow separation regions, due to an erroneous evaluation of $y_{max}$ [10][22]. This ambiguity due to physical flow features is shown by the points $a$ and $b$ of ray $y_2$ in figure 3 and to prevent it, the Dagani-Schiff adaption to the model, determines $F_{max}$ once the value of $F(y)$ drops to 90% of the first detected maximum [22].

Altogether, the Baldwin-Lomax model with the Degani-Schiff modification has been successfully used to study slender body, compressible, vortex dominated flows [10] and is still in use due to its ease of implementation and minimum requirements [20].



*Figure 3. Crossflow flow structure with details for the Degani-Schiff formulation. [22]*

### 3.2.2  One-equation EVM

Although zero-equation models are still in use today, they exhibit several shortcomings that highly limit their applicability. This type of models are not local, meaning that the equation at one point in the domain, depends on the solutions found at other points, and are therefore only suited for simple geometries having smooth, structured grids [23]. Besides, they frequently show a weaker performance in more complex cases such as separated boundary layers and their use for the study of vortical flows should be carefully considered.

In one-equation models these limitations have been addressed with the specification of a length scale by means of an algebraic formula (similar to the zero-equation models) and the addition of one transport equation.

Out of the several examples of this type of models, the Spalart-Allmaras [23] is one of the most recent and widely used. The model involves a transport equation, shown in equation 7, for a parameter based on the kinematic eddy viscosity ($\tilde{v}$) that relates to the dynamic eddy viscosity by equation 8.

$$\frac{\partial(\rho\tilde{v})}{\delta t} + div(\rho\tilde{v}U) = \frac{1}{\sigma_v}div\left[(\mu + \rho\tilde{v})\,grad(\tilde{v}) + C_{b2}\rho\frac{\partial\tilde{v}}{\partial x_k}\frac{\partial\tilde{v}}{\partial x_k}\right] + C_{b1}\rho\tilde{v}\overline{\omega} - C_{w1}\rho\left[\frac{\tilde{v}}{ky}\right]^2 f_w \qquad (7)$$

$$(I) \qquad (II) \qquad\qquad\qquad (III) \qquad\qquad\qquad (IV) \qquad\quad (V)$$

$$\mu_t = \rho\tilde{v}f_{v1} \qquad\qquad (8)$$

In equation 7, the term $(III)$, corresponds to the transport of $\tilde{v}$ by turbulent diffusion, the terms in block $(IV)$ represent the rate of production of $\tilde{v}$ as function of the local mean vorticity, and the term $(V)$ is the rate of dissipation of $\tilde{v}$ as function of a length scale ($ky$) that depends on the distance to the wall and the von Karman constant [23]. The term, $f_{v1}$ in equation 8 is a wall-damping function that depends on ($\tilde{v}/v$), i.e., the ratio between the kinematic viscosity parameter and the kinematic viscosity, and tends to unity at high Reynolds numbers and zero at the wall region [9]. Further wall-damping functions were also developed and included in the transport equation to maintain the model's behaviour throughout the different regions of the boundary layer, as well as a series of constants specifically calibrated for external aerodynamic flows [9][23].

The result is a robust and easy to implement model that has been extensively validated for external flows in aerospace applications and has been shown to provide appropriate performance in cases with boundary layers subjected to adverse pressure gradients. It presents, however, a general difficulty to define the length scale in cases with complex geometries and rapidly changing flows with high levels of anisotropy [9], and the general nature of its constants make it unsuitable for general-purpose CFD.

### 3.2.3 Two-equation EVM

Regardless of their relative success, the inherent features of one-equation models, i.e., the use of only one transport equation and the need of a priori knowledge of the length scale for each particular case, make them inappropriate to accurately describe the details of general turbulent motions.

A step forward is taken by the two-equation models that incorporate a second transport equation to further determine both the turbulent velocity and length scales, representative of large-scale turbulence, and better comply with the general description of the eddy-viscosity as the product of these scales [24]. At its core, this type of model involve more realistic descriptions of the dynamics of turbulence, and most of them focus on the mechanisms that affect the transport of turbulent kinetic energy ($k$) [9][24]. The choice of the remaining variable is not unique, and the most widely validated models in this category solve either for the dissipation rate $\varepsilon$ or the dissipation rate per unit of turbulent kinetic energy, i.e., $\omega = \varepsilon/k$, as part of the $k - \varepsilon$ and $k - \omega$ model formulations [25]. Given these features, these models are considered complete, meaning that they can be used to study the properties of a given turbulent flow without knowledge of its turbulent structure [26].

The standard $k - \varepsilon$ model [27], includes two transport equations, one for the turbulent kinetic energy ($k$), given in equation 9 and one for its dissipation per unit of mass ($\varepsilon$) in equation 10. The model also defines, through dimensional analysis, the required velocity and length scales to specify the eddy viscosity, as given by equation 11.

$$\frac{\partial(\rho k)}{\delta t} + div(\rho k U) = div\left[\frac{\mu_t}{\sigma_k}\, grad(k)\right] + 2\mu_t s_{ij} \cdot s_{ij} - \rho\varepsilon \qquad (9)$$

$$(I) \qquad (II) \qquad\qquad (III) \qquad\qquad (IV) \qquad (V)$$

$$\frac{\partial(\rho\varepsilon)}{\delta t} + div(\rho\varepsilon U) = div\left[\frac{\mu_t}{\sigma_\varepsilon}\, grad(\varepsilon)\right] + C_{1\varepsilon}\frac{\varepsilon}{k} 2\mu_t s_{ij} \cdot s_{ij} - C_{2\varepsilon}\rho\frac{\varepsilon^2}{k} \qquad (10)$$

$$(I) \qquad (II) \qquad\qquad (III) \qquad\qquad (IV) \qquad (V)$$

$$\vartheta = k^{1/2} \qquad l = \frac{k^{3/2}}{\varepsilon} \qquad\qquad (11)$$

$$\mu_t = \rho C_\mu \frac{k^2}{\varepsilon}$$

The terms $(III)$, $(IV)$ and $(V)$ of equations 9 and 10 represent the transport by diffusion, the rate of production and the rate of dissipation of $k$ and $\varepsilon$. Here $\sigma_k$ and $\sigma_\varepsilon$ in the term $(III)$ of these equations correspond to Prandtl numbers which connect the diffusivities of $k$ and $\varepsilon$ to the eddy viscosity $\mu_t$, and $s_{ij}$ in the term $(IV)$ is the mean-strain-rate tensor of a fluid element. The model at its core fixes a close link between $k$ and $\varepsilon$ and assumes that the production $(IV)$ and dissipation $(V)$ of $\varepsilon$ are proportional to the production and dissipation of $k$, to ultimately avoid non-physical, negative values of turbulent kinetic energy if it decreases [9].

Equation 10 contains the constants $C_{1\varepsilon}$ and $C_{2\varepsilon}$ which are closure coefficients used by the model due to the high complexity of the exact $\varepsilon$ transport equation and the difficulty to measure some of its terms. In addition, $C_\mu$ in equation 11 is a dimensionless constant established from the nearly constant value it acquires in the logarithmic region of equilibrium flow.

Altogether, the classic version of the model contains five adjustable constants, i.e. $C_\mu$, $\sigma_k$, $\sigma_\varepsilon$, $C_{1\varepsilon}$ and $C_{2\varepsilon}$, that are tuned for a wide range of turbulent flows and allow it to achieve accurate calculations for a wide variety of thin shear layer and recirculating flows without the need of a case-by-case adjustment of the constants [9]. The model is also the most widely used and validated, including Launder & Spalding [27], Jones & Launder [28] and Launder & Sharma [29] to mention some.

However, the model as given tends to overestimate the shear stress in the viscosity affected region of the boundary layer and delay its separation for cases with adverse pressure gradients such as curved walls. It also has complications when dealing with swirling flows and massively separated areas due to the prediction of inappropriate turbulent length scales and a consequent eddy viscosity. These shortcomings make its use in aerospace applications not entirely recommended and importantly limit its use for the study of vortex phenomena [9][30]. In this case, the problem is attributed to the empirical way the transport equation of the turbulent dissipation rate is modelled [25] and to the wrong assumption of $C_\mu$ in equation 11 as constant along the entire boundary layer, as both experimental and numerical (DNS) data, have indicated a reduction in its value in the near-wall region $(0 \le y^+ \le 100)$ [24].

There are two identified ways to deal with this last issue; one uses a series of damping functions that reduce the value of $C_\mu$ in the near-wall region and the other relies on empirical wall-functions based on the general behaviour of near-wall flows, that bridge the near-wall region, and concern only a value of $C_\mu$ away from the wall (inertial sublayer), where the assumption of a constant value correctly applies. The models that abide by the first approach are known as Low-Reynolds-Number

(LRN) models and differ from their High-Reynolds-Number (HRN) counterparts, i.e. the latter approach, in that they need to be resolved down to the wall. The Reynolds number considered here does not refer to the global Reynolds number, but the local turbulent Reynolds number $Re_l = \vartheta l / v$ formed by a turbulent fluctuation and turbulent length scale [15][24][27][28]. The use of these functions has been shown to improve the treatment of the near-wall region; however their general nonlinear nature tends to add stiffness to the formulation of the model and therefore to affect its convergence properties [31].

Besides, the versatility of the classical $k - \varepsilon$ model allows it to be easily modified and several versions have been developed that are capable of addressing some of the mentioned limitations including Shih et al. [30] and Yakhot et al. [32]. The first one is based on a method known as the renormalisation group method (RNG) that heavily relies on statistical analysis and mathematical formalisms to systematically remove the smallest scales of turbulence from the governing equations and expresses them in terms of larger scale motions and a modified viscosity. Besides, this version of the model explicitly determines the value of its respective constants as part of the RNG method [9][32] and its formulation does not require the use of damping functions in the near-wall region. The model has shown to achieve improved predictions on wake flows when compared to the standard version but tends to overpredict the eddy viscosity, i.e., the model is highly dissipative, and showed limitations when predicting separation and reattachment points in some studied cases [33].

The second approach is known as $k - \varepsilon$ Realisable [30] and is based on the application of realizability constraints to the Reynolds stresses. The constraints force both the normal stresses to remain positive, and the correlation coefficients for the shear stress not to exceed one, and make them consistent with the physics of turbulent flows [9][30]. The other key differences to the standard version include the use of a modified transport equation for the dissipation rate that is based on the mean vorticity fluctuation and is more physically related to the original $\varepsilon$ equation, as well as a new realisable formulation for the coefficient $C_\mu$ which makes it variable along the boundary layer rather than a constant. The model as a whole has shown to outperform the standard $k - \varepsilon$ model in a wide range of tested cases, and it's more recommended for flow topology studies [30].

Another type of two-equation model is the $k - \omega$ [34] that expresses the turbulent scales and the eddy viscosity in terms of the turbulent kinetic energy ($k$) and the specific dissipation rate ($\omega$) as given in equation 12

$$\vartheta = k^{1/2} \qquad l = \frac{k^{1/2}}{\omega} \tag{12}$$

$$\mu_t = \rho \frac{k}{\omega}$$

The model uses the two transport equations, i.e., equation 13 and 14, for $k$ and $\omega$.

$$\frac{\partial(\rho k)}{\delta t} + div(\rho k U) = div\left[\left(\mu + \frac{\mu_t}{\sigma_k}\right) grad(k)\right] + \left[2\mu_t s_{ij} \cdot s_{ij} - \frac{2}{3}\rho k \frac{\delta u_i}{\delta x_j}\delta_{ij}\right] - \beta^* \rho k \omega \tag{13}$$

$$(I) \qquad (II) \qquad\qquad (III) \qquad\qquad\qquad (IV) \qquad\qquad (V)$$

$$\frac{\partial(\rho \omega)}{\delta t} + div(\rho \omega U) = div\left[\left(\mu + \frac{\mu_t}{\sigma_\omega}\right) grad(\omega)\right] + \gamma_1\left[2\rho s_{ij} \cdot s_{ij} - \frac{2}{3}\rho \omega \frac{\delta u_i}{\delta x_j}\delta_{ij}\right] - \beta_1 \rho \alpha \tag{14}$$

$$(I) \qquad (II) \qquad\qquad (III) \qquad\qquad\qquad (IV) \qquad\qquad (V)$$

As in the transport equation of $\varepsilon$ (equation 10), the terms $(III)$, $(IV)$ and $(V)$ of equations 13 and 14 respectively represent the transport by diffusion, the rate of production and the rate of dissipation of $k$ and $\omega$. The model is composed of five closure coefficients, i.e., $\sigma_k$, $\sigma_\omega$, $\beta^*$, $\beta_1$ and $\gamma_1$, that are assumed constant and are calibrated based on experimental observations for decaying, homogeneous, isotropic turbulence to satisfy the law of the wall, i.e., the linear variation of velocity with the logarithm of distance from the surface [9][26][34].

The formulation, as presented, integrates the equations down to the wall (through the viscous sublayer) and obtains the turbulent scales without the need of wall-damping functions, further contributing to the stability of the model [31]. In this regard, it has been proven that both the standard version and the LRN one, achieve similarly accurate results for a set of conducted tests [35]. A set of conditions have also been set in the model to avoid non-physical results at the near-wall grid point including the assumption of $k$ as zero and the forced fulfilment of the analytical solution of equation 14 for $\omega$ [36].

$$\omega = \frac{6\mu}{\rho \beta_1 y^2} \tag{14}$$

This allows the model to show improved accuracy for cases with attached boundary layers in adverse pressure gradients, compressible boundary layers and free shear flows, and to provide better results for the simulation of transition with the pertinent modifications [34][37]. The model also performs significantly better than the $k - \varepsilon$ model under adverse pressure gradients. Unfortunately, its results tend to be highly sensitive to the assumed free-stream value of $\omega$ and this shortcoming constraints its application for the study of external aerodynamics cases [31][36].

In Menter [31], efforts were made to overcome this limitation that resulted in the development of the Base Line (BSL) model and the further improved Shear-Stress-Transport (SST) model. The SST model leverages some of the features of both $k - \omega$ and $k - \varepsilon$ models, which ultimately result in the same robustness of the standard $k - \omega$ model with a small added computational cost. To perform with one set of equations, the model considers a modified version of the $k - \varepsilon$ model that transforms it into a $k - \omega$ formulation. At its core, the formulation benefits from the better performance of the $k - \varepsilon$ model in the free stream to accurately treat the region away from the wall, while the improved capabilities of the $k - \omega$ model in the near-wall region provide a better description of the boundary layer.

A blending function is used to smooth the transition between the two models as the distance from the wall increases. In this case the function i) tends to one at the wall, ii) tends to zero at the farfield and iii) transitions at around half the distance between these two points, and does it without user interaction or a priori knowledge of the flowfield. This approach allows the model to achieve a similar performance to the standard $k - \omega$ model in boundary layers subjected to adverse pressure gradients, without the dependency on free-stream conditions and has shown to be identical to the $k - \varepsilon$ when dealing with free shear layers. The BSL model was found to predict poorly the separation region of cases with severe adverse pressure gradients which motivated further modifications to the model and gave the impetus for the development of the SST version [31]. The SST version further accounts for the transport of the principal turbulent shear stress and does it through a modified definition of the eddy viscosity in the BSL model, which assumes a proportional relation between the shear stress and the turbulent kinetic energy. The model also uses closure coefficients that are computed by blending the corresponding constants of the $k - \varepsilon$ and the $k - \omega$ models and have been refined from experience [38][39].

The $k - \omega$ SST model has ultimately led to significant improvements in the prediction of boundary layer flows under adverse pressure gradients and has been successfully used not only for aerodynamics applications such as the analysis of complete aircraft configurations but also as part of improved DES formulations given its improved separation prediction capabilities [39].

### 3.2.4 Reynolds Stress Transport Models

Despite the considerable performance improvement achieved by two-equation EVM's in a wide range of case studies, this type of model still demonstrate limitations in cases involving curved walls and swirling flows. The errors are attributed to the additional interactions between the mean strain rate and the Reynolds stresses produced in these flows, and the inherent inability of these models to correctly predict the resultant anisotropy of the normal Reynolds stresses, given the assumption of turbulence isotropy made by the Boussinesq approximation [25][27]. A way to rectify this limitation relies on the use of higher-order closures that allow a more accurate description of the features of turbulent flows such as the Reynolds stress equation models (RSM)[40]

At its core, the method includes a set of six exact transport equations for the Reynolds Stresses themselves (three normal and three shearing stresses), which allow to account for their directional effects, i.e. anisotropy, and have the form presented in equation 15.

$$\frac{\delta \overline{u_i u_j}}{\delta t} + C_{ij} = P_{ij} + D_{ij} - \varepsilon_{ij} + \Pi_{ij} + \Omega_{ij} \tag{15}$$

Equation 15 keeps the form of the transport equations included in the formulation of two-equation EVM's, with the terms $P_{ij}$, $D_{ij}$ and $\varepsilon_{ij}$ representing the rate of production, and transport by diffusion and dissipation of the Reynolds stresses, but includes two new physical processes: the pressure strain interaction term ($\Pi_{ij}$) and the rotation term ($\Omega_{ij}$).

The transport equations as presented are not closed, and the method requires models for $D_{ij}$, $\varepsilon_{ij}$ and $\Pi_{ij}$, expressed in terms of known or determinable quantities, to close the system [25]. In Launder et al. [41] the formulation of a series of models that achieve this are presented, and only their general approximations will be mentioned next for the sake of simplicity.

The diffusion term is processed based on the assumption that the rate of transport of Reynolds stresses by diffusion is proportional to the gradients of Reynolds stresses, as part of the Generalised Gradient Diffusion Hypothesis (GGDH), given by equation 16,

$$D_{ij} = \ div\left(\frac{\mu_t}{\rho\sigma_k} grad(\overline{u_i u_j})\right) \tag{16}$$

with $\sigma_k = 1$ and $\mu_t$ usually taken as equation 11. The dissipation rate is typically modelled using equation 17, with the assumption of isotropy in the small dissipative scales at high Reynolds numbers.

$$\varepsilon_{ij} = \frac{2}{3}\varepsilon\delta_{ij} \tag{17}$$

In this case, the term $\varepsilon_{ij}$ is applied to only affect the normal Reynolds stresses by using the Kronecker delta and introduces an additional transport equation for the dissipation of kinetic energy ($\varepsilon$) which is commonly equal to the one from the standard $k - \varepsilon$ model in equation 10 [9][25].

Finally, the pressure strain interaction is usually decomposed into two terms that account for the two physical processes in which it influences the Reynolds stresses: 1) the mutual interaction between turbulent eddies and 2) the interaction between turbulent fluctuations and the mean flow strain [41].

The first one is known as "slow" and reduces anisotropy of the eddies while the second mechanism is called "rapid" and is responsible for the formation of eddies that oppose the production of anisotropy from turbulent eddies. These processes help redistribute the energy between the normal Reynolds stresses to make them more isotropic and reduce the Reynolds shear stresses.

Altogether, in the RSM method, seven transport equations are solved that include six for the Reynolds stresses and one for the dissipation rate. Regardless of the added complexity, this type of model is generally considered as the "simplest" that allows a complete description of both the mean flow properties and the Reynolds stresses without a case by case adjustment.

When compared against the $k - \varepsilon$ model, the method has shown improved predictions in aerospace applications with more accurate predictions of the onset of separation. However, it is not as widely validated or used in industry due to its added complexity and computational cost. The model can also show similar limitations to the $k - \varepsilon$ model, given the transport equation of $\varepsilon$ in its formulation [9].

## 3.3 The Computational Mesh & Mesh Adaption

The computational meshes for all four test cases were structured. Figure 4 presents a schematic representation of the computational flow domain with the principle boundary conditions applied to each boundary surface except the far-field outer boundary which, for the benefit of clarity, is not shown. The model is for only half of the flow field with a symmetry plane imposed on the basis that at the angles of attack being computed, the experimentally measured flow field is symmetric about the *y = 0* plane, passing through the centre of the body.
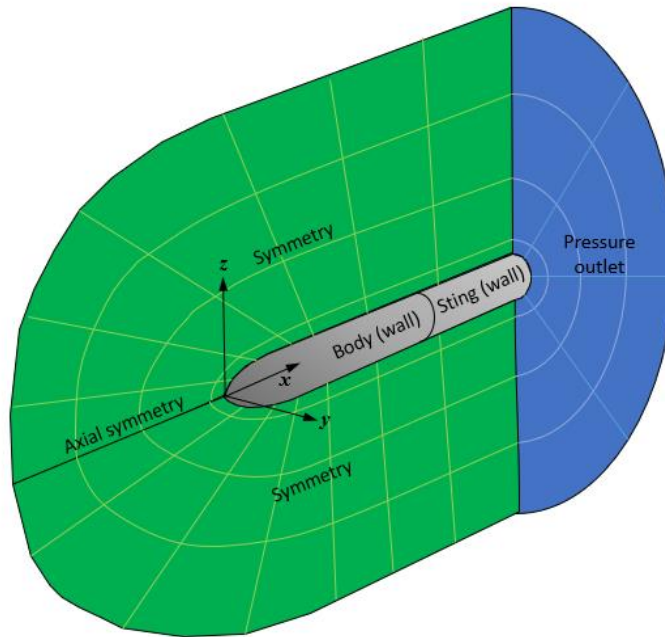


*Figure 4: The structured meshing strategy.*

A symmetry boundary condition was applied to the upper and lower symmetry surfaces (shown in green), while the body surface and an extended rear surface behaving like a sting geometry were given an adiabatic (no heat transfer) wall boundary condition. The sting extension, which was not intended to match the actual sting configuration in the wind tunnel test, was added to ensure that the boundary condition on the outflow plane (shown in blue) - a pressure outflow boundary formulation, was far behind the forebody. This was deemed necessary because the actual pressure field on this plane would not be constant. The residual shock wave and, to a lesser extent, the body wake will

impose pressure variations across the outflow plane, so locating this at least one body length downstream will ensure that, for the transonic case in particular, the upstream influence of this relatively minor error does not significantly affect the flow solution in the locality of the body itself.

An axially symmetric line boundary condition was applied to the line emanating upstream of the nose tip, which represents a collapsed surface and requires special mathematical treatment to correctly compute the flow in this region. The outer flow boundary, which is not shown in figure 4, used a non-reflective transmissive boundary condition in the case of the supersonic flow cases, and a pressure far-field boundary condition for the subsonic test case (case 3). The outer flow boundary was located at a distance from the body at which the influence of the body would be negligible. For the supersonic cases this means ensuring that the nose shock wave is well within the outer boundary at all angle of attack conditions of interest (see figure 3). For the subsonic test case, this meant locating the outer boundary at a minimum of 10x the body length away from the body surface due to that fact that in subsonic high Mach number flow, the influence of a body can extend a considerable distance.

The governing compressible Reynolds Averaged Navier-Stokes equations were solved for steady flow with spatial accuracy set to third order using the MUSCL variable extrapolation method, with the Roe approximate Riemann solver for the capturing of the shock waves. Turbulent kinetic energy and dissipation were computed to second order accuracy. The solution process involved initializing the flowfield to freestream conditions everywhere except the body surface, where all three components of velocity are zero. One thousand explicit iterations were performed with a CFL number of 0.75, to get the solution converging before implicit iterations with a CFL number of 15 converged the solution to completion.

For all four test cases a mesh sensitivity study was performed. Table 2 presents details of the mesh density details, where the finest mesh was found to provide mesh converged (forces and moments convergence to four significant figures, and convergence of the surface pressure distribution to within $\Delta C_p \sim \pm 0.0005$) in all cases. For all meshes, the first cell height adjacent to the body surface as set at $1 \times 10^{-5}$ times the afterbody cross-sectional diameter, $D$, as previous studies have shown that this gives a wall $y^+$ value of the order of 1 across the body surface, except the region very close to the nose tip, where the experimental boundary layers are laminar in reality.

Once the converged result was obtained on the finest mesh, this was then further refined using feature adaptive mesh refinement and the solution continued until convergence was re-established on this adapted mesh. This refinement was done using pressure gradient (greater than 200 Pa/m) as the refinement metric, such that refinement was focussed across the shock wave, and in the vortices. Figure 5 presents, for test case 1, at zero angle of attack, the final refined mesh on the upper symmetry plane as an example, and the corresponding density contours demonstrating the sharpness with which the nose shock wave is resolved.

| Mesh | Axial cells | Radial cells | Circumferential cells | Total cell count |
|---|---|---|---|---|
| Structured coarse | 90 | 45 | 45 | 182,250 |
| Structured intermediate 1 | 90 | 90 | 90 | 729,000 |
| Structured intermediate 2 | 120 | 90 | 90 | 972,000 |
| Structured fine | 120 | 120 | 120 | 1,728,000 |

*Table 2: Mesh size details (subsequent mesh adaption was performed only on fine mesh).*
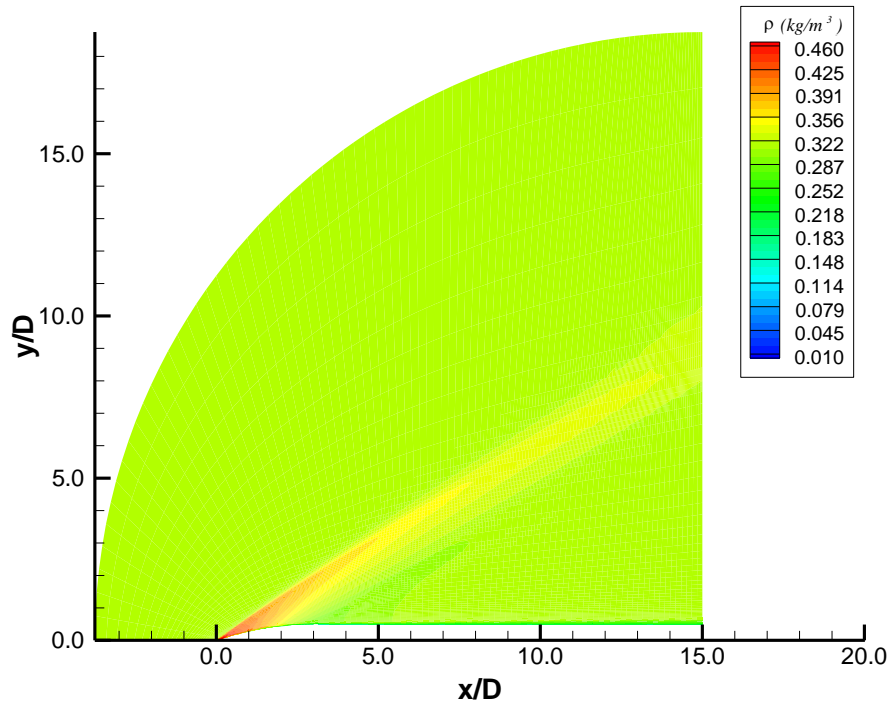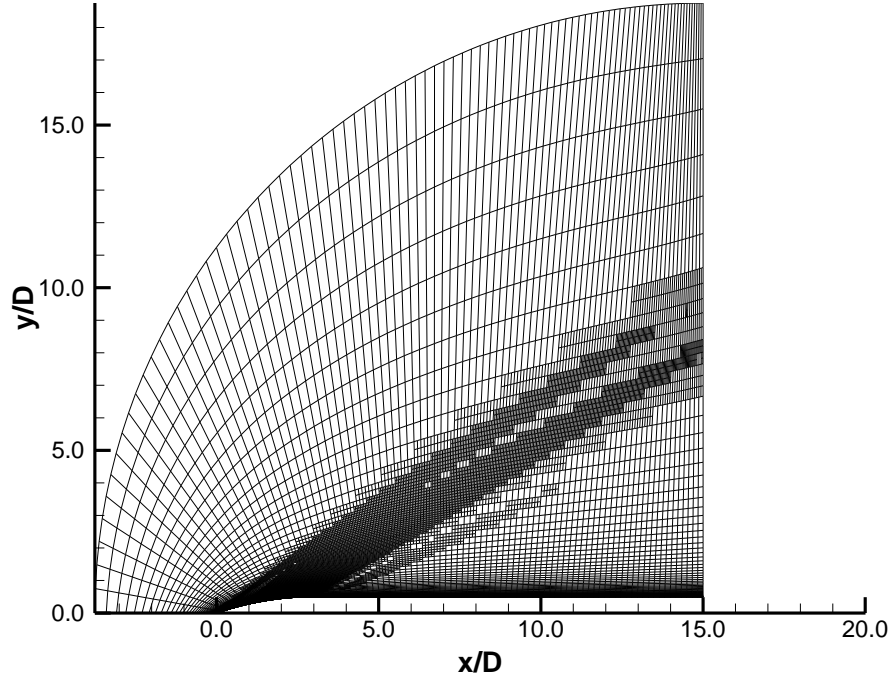
*Figure 5: Example adapted mesh and corresponding computed density contours, M=2.0. α=0°,*
*Re_D=1.2x10^6.*

# 4. Results

## 4.1   B2, M=2.0, $\alpha = 0^o$ Test Case

Test case 1 is the $\alpha = 0^o$ B2 test case, which is therefore axisymmetric. The grid for this case was also axisymmetric, although it was recognised that a 2D plane could have been more efficiently computed with the axisymmetric formulation of the flow equations. The results using either approach, however, would be identical. Figure 6 presents a comparison of the experimentally measured surface pressure distribution with those obtained from two eddy viscosity turbulence models, the Reynolds Stress model and also the two scale resolving methods – Scale Adaptive Simulation and Detached Eddy Simulation. For this zero incidence case, where there is no boundary layer separation at all, it is seen that all turbulence methods have been equally successful in capturing the surface pressure levels across the body, and by inference the pressure drag contribution, to within the limits of experimental accuracy.

Figure 7 presents the comparison, with the experimentally measured value, of the predicted axial force coefficient, $C_A$ , which for this case is equivalent to the drag coefficient, obtained using all of the turbulence approaches tested. Since the pressure contribution to this force is likely to be accurately resolved by each method, the differences seen here are entirely due to the resolution of the surface skin friction contribution – that is, the resolution of the turbulence boundary layers along the body. The three methods which seem to most successfully (within the limits of experimental accuracy) are the $k$-$\omega$ SST turbulence model and the Scale Adaptive and Detached Eddy Simulation methods. What is a surprise, perhaps, is that the Reynolds Stress Model overpredicts the axial force by about 15%, whereas the zero order Baldwin – Lomax model overpredicts by only 5%. None of the turbulence methods underpredict the axial force coefficient.
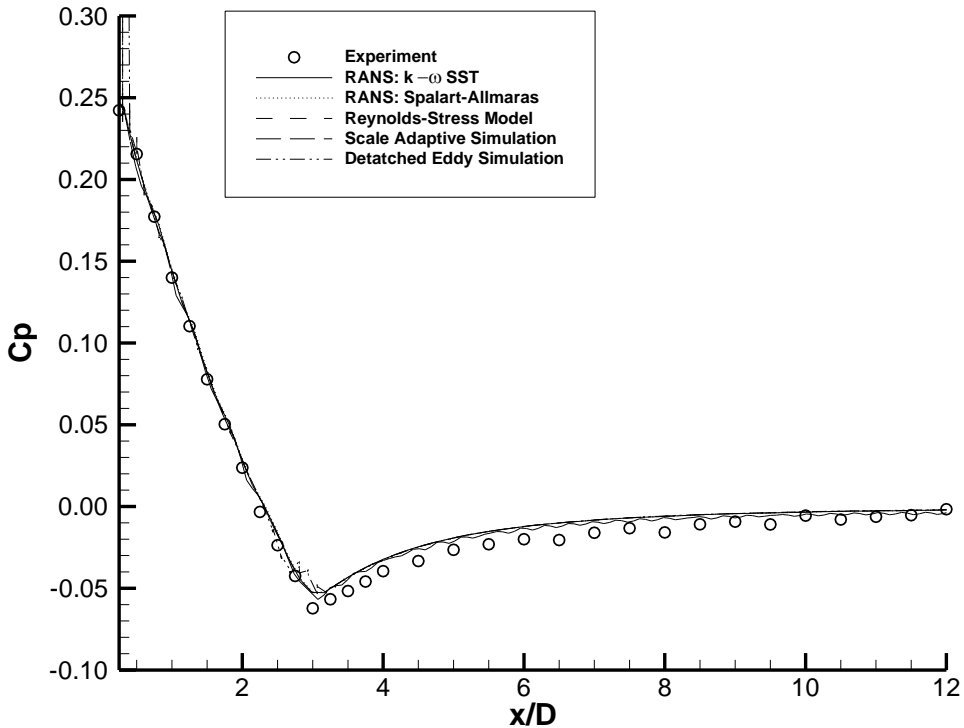


*Figure 6: Comparison of measured and predicted surface $C_p$. B2, M=2.0, $\alpha=0^o$, $Re_D=1.2x10^6$.*
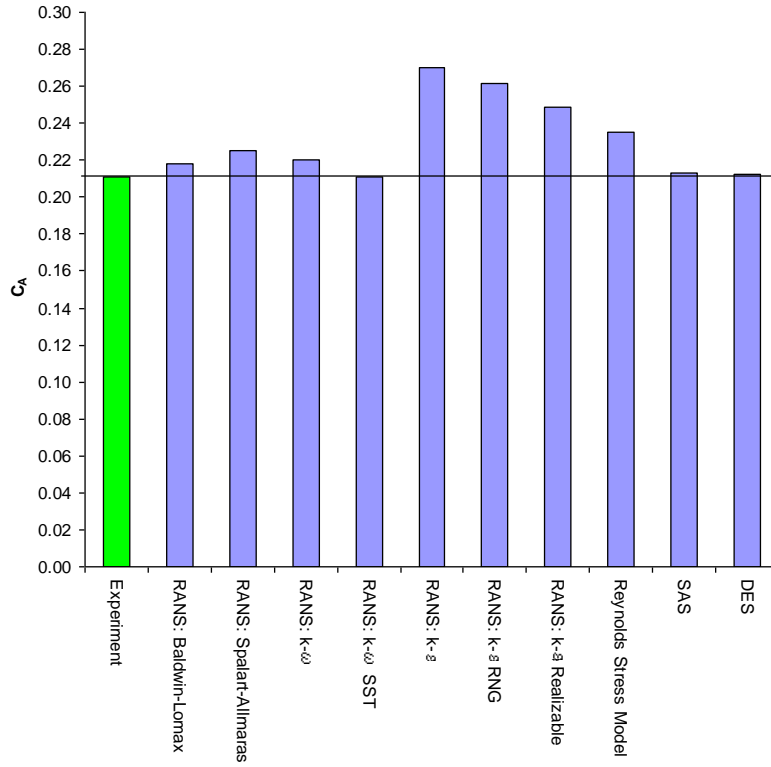
*Figure 7: Comparison of measured and predicted axial force coefficient. B2, M=2.0, α=0°,*
*Re$_D$=1.2x10$^6$.*

Figure 8 provides more insight into this analysis by comparing the experimentally measured turbulent boundary profiles with each of those obtained using the different numerical turbulence methods for five *x* stations down the length of the body. On the left side of the figure are plotted the comparisons for the eddy viscosity, RANS turbulence models, while on the right side are plotted the corresponding comparisons for the higher fidelity methods, and the *k-ω* SST model. At *x/D*=3, as the supersonic flow over-expands past the junction of the ogival nose and the cylindrical afterbody, the boundary layer has been processed by the large adverse pressure gradient on the nose. The Bladwin-Lomax model resolves the inner boundary layer velocity relatively well, but fails to capture the velocities at the top of the boundary layer, and in the freestream where there is too much dissipation. The standard *k-ω* model also performs poorly compared with the rest, giving too high velocities in the inner region and too low velocity towards the top of the boundary layer. The *k-ω* SST and the Spalart-Allmaras models also overpredict the velocities in the boundary layer, while the *k-ε* based models all slightly underpredict the velocities. Overall the best of the RANS based models at this *x/D* station appears to be the *k-ε* Realizable model. Scale Adaptive Simulation is seen to predict velocities that are up to 20% too high compared with the experimentally measured values at the same height above the surface. Detached Eddy Simulation appears to provide a better prediction, but the best result seems to be that from the Reynolds Stress Model, which is marginally better than that obtained from the *k-ε* Realizable model.

The same trends are seen in the boundary layer predictions at *x/D*=5, where the pressure gradient is favourable. Here the Baldwin Lomax model predicts velocities too low in the inner boundary layer, and too high in the outer boundary layer. The *k-ε* based models underpredict the velocity at a given height in the boundary layer by up to 10%, while the other RANS models generally overpredict the velocity by up to 20%. Here the *k-ε* Realizable and Spalart-Allmaras models do the best out of the RANS models. Of the higher fidelity methods, the Reynolds Stress Model provides the best overall prediction of the boundary layer at this station, followed by Detached Eddy Simulation.
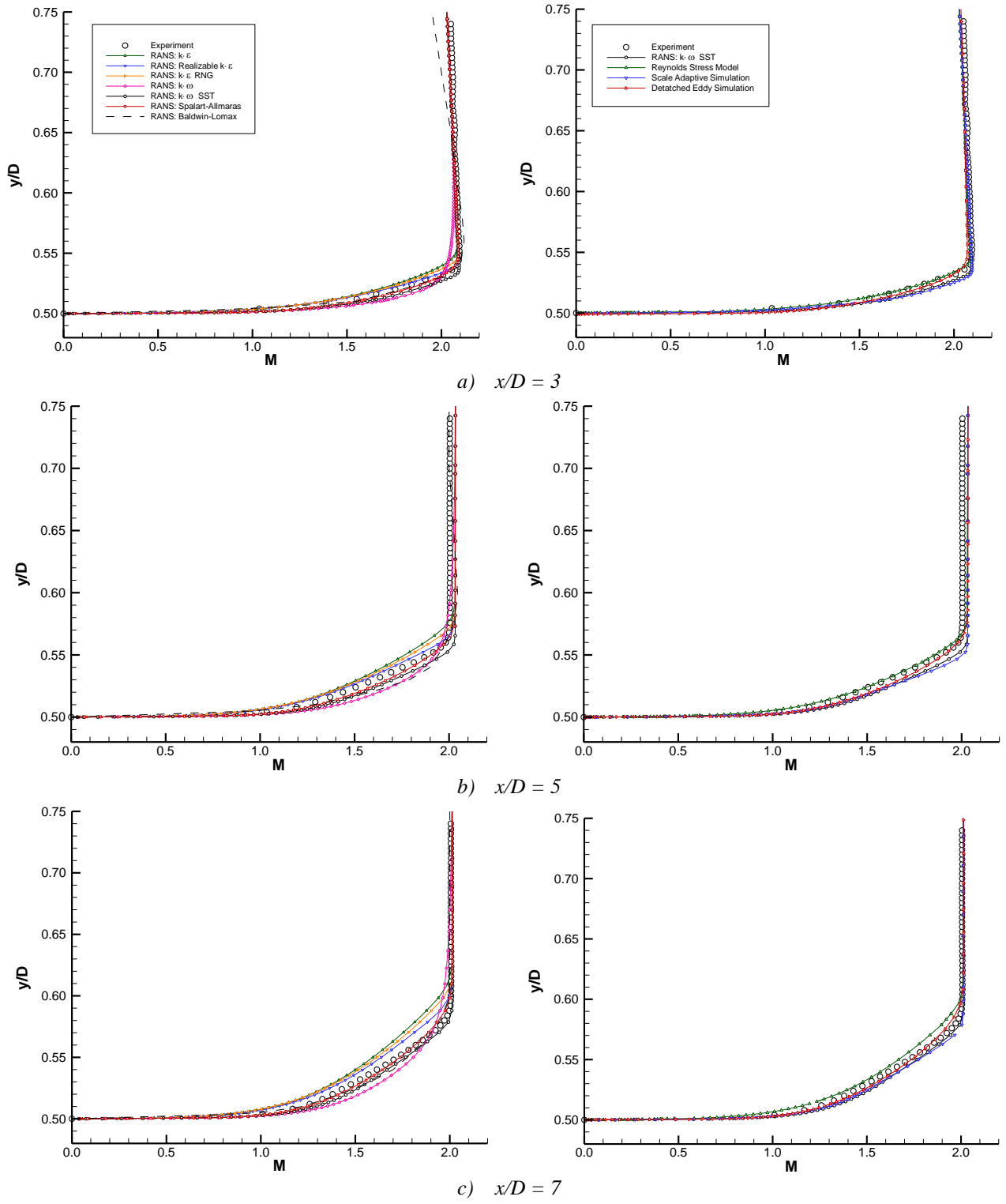
*a) x/D = 3*

*b) x/D = 5*

*c) x/D = 7*

*Figure 8: Comparison of measured and computed boundary layer profiles, B2, α = 0ᵒ, M=2.0,*
$Re_D=1.2x10^6$.

*d)   x/D = 9*





*e)   x/D = 12*
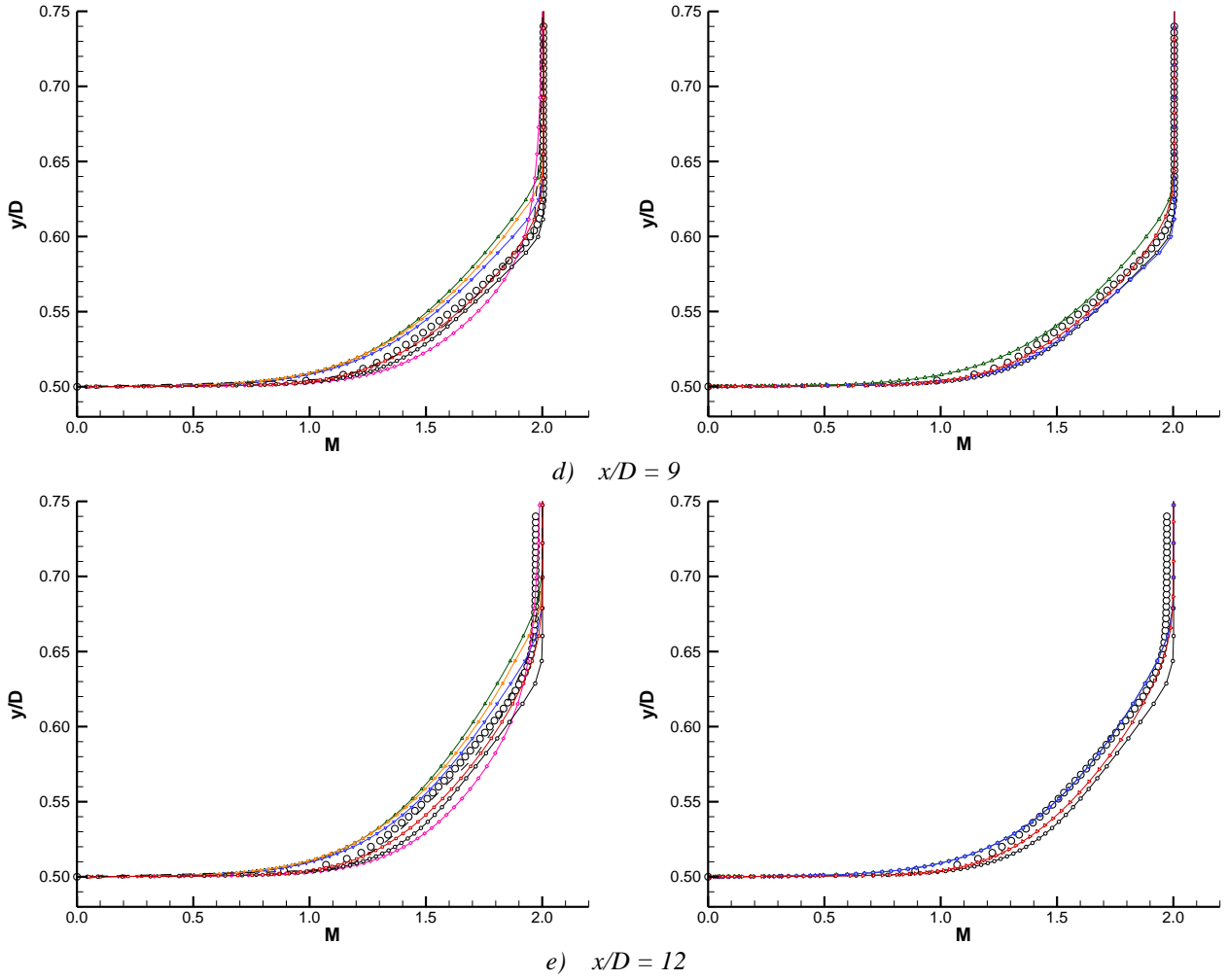
*Figure 8:  Comparison of measured and computed boundary layer profiles, B2, $\alpha = 0^o$, M=2.0, $Re_D=1.2x10^6$ (concluded).*

These trends are generally the same at station *x/D*=7, where the pressure gradient is now neutral and the boundary layer is seen to be growing more rapidly. However, it is now the Spalart-Allmaras model which provides the closest match to the experimentally measured boundary layer, with the *k-ε* based models underpredicting the local velocities more significantly, by up to 20%. The standard *k-ω* model performs the worst, while the SST version does a good job with predicted velocities within 5% of those measured in experiment. Of the higher order methods, it is now the Detached Eddy Simulation and the Solution Adaptive Simulation which seems to provide the best match with experiment, which is what might be expected. At this station the Reynolds Stress Model velocities are too low, at any given height above the surface, with a discrepancy of up to 10%.

These trends are the same for stations *x/D* = 9 and 12 as well, though the percentage discrepancies begin to increase. Taking all of the evidence into account, the *k-ε* Realizable seems to be the best RANS model at predicting the turbulent boundary layer evolution over this class of axisymmetric body, with the *k-ω* SST and Spalart-Allmaras models generally within 10% of the measured velocity profile. The standard *k-ω* is consistently the worst, with discrepancies of up to 25% from the measured velocity value. While the Reynolds Stress Model seems to provide the best predicted velocity profiles in the region following the highest adverse pressure gradient, the scale resolving turbulence simulation methods do the best job overall, with Scale Adaptive Simulation providing the most accurate numerical boundary layers on the cylindrical afterbody.

## 4.2   B2, M=2.0, $\alpha = 10^o$ Test Case

At $10^o$ angle of attack in a Mach 2.0 airflow the boundary layer which forms on the windward side of the B2 body will experience a growing adverse pressure gradient as it passes onto the leeward side. The boundary layer will therefore undergo crossflow separation from a three-dimensional separation line on the smooth windward surface of the body. At $\alpha = 10^o$, the experimental results showed that the consequent vortices developed in a steady, symmetric pattern as shown in figure 1. For these conditions the steady RANS approximation and a symmetric half model with symmetry plane boundary conditions will therefore be valid.

Figures 9, 10 and 11 present the comparison between the experimentally measured total pressure contours and those computed using the different turbulence methods, in crossflow *(y-z)* planes at *x/D* = 5, 7 and 9 respectively. Figures 12, 13 and 14 then present the corresponding comparisons of local Mach number at the same planes, while figures 15, 16 and 17 do the same for the contours of local flow angle. The comparison of the total pressure contours in the crossflow station *x/D* = 5 is presented in figure 9. The experimentally measured contours are at the top left-hand side. In this plot it is seen that the data does not extend out radially beyond 0.8*D*. This is due to the size of the extent of the traverse of for the 5 hole probe used in the experiment. The data does, however, extend almost all the way to the model surface. At this axial location there is seen to be a boundary layer separation at around $\phi = 110^o$, but the shear layer has not yet rolled up to form a fully developed vortex. All of the turbulence methods tested appear the have resolve the flow structure correctly, with only minor differences in the size and structure of the separated flow prior to primary reattachment on the windward symmetry plane. In particular there are differences in the size and level of the suction region within the separated shear layer. The Baldwin-Lomax / Degani-Schiff model appears to be the least able to resolve this low pressure region, while the standard $k$-$\omega$ model seems to be too dissipative at the edge of the boundary layer and separated shear layer. The method which most closely approximates the experimental measurements is the $k$-$\varepsilon$ Realizable model. All of the other two-equation turbulence models, except the standard $k$-$\omega$ model, and the unsteady higher fidelity models provide reasonably accurate predictions compared with the experimental result.

At *x/D* = 7, presented in figure 10, the experimental measurement shows that by this station the shear layer is rolled up into a vortex, though not necessarily fully developed. There is also evidence of a secondary separation and associated vortex that sits under the primary vortex. None of the numerical predictions resolved a distinct primary vortex core seen in the experimental measurement, or any significant secondary separation and associated secondary vortex. This suggests that either the turbulent dissipation is too high in all of these turbulence models and simulation approaches, or the experimental flow is sensitive to the initial region of laminar flow that exists up to *x/D*=0.5, where the transition strip is located. If this laminar boundary layer in the experimental flow undergoes separation before this fixing location, transition will occur in the shear layer, and the downstream vortex will have the structure and strength of a full turbulent flow. Without further information, however, this must remain speculation. The overall size and shape of the forming primary vortex is reasonably well captured by all turbulence methods, except perhaps the standard $k$-$\omega$ model which, again, appears to dissipate the vortex edge.

Further downstream at *x/D*=9, presented in figure 11, the experimental total pressure contours reveal a fully developed primary vortex and a small secondary vortex between the primary feeding sheet (shear layer) and the primary vortex. At this station there is seen to be a considerable level of difference in the resolution of the leeside vortical flow. All of the numerically predicted primary vortices do exhibit a distinct core, and all successfully resolve a secondary separation below the primary vortex, but only a few resolve a significant secondary vortex. While the experimentally measured primary vortex was very circular in structure, that evolved using the Baldwin-Lomax based model appears to be more elliptic and unrepresentative of the experimental vortex, but the method does successfully resolve the secondary vortex in the right place and strength. The Spalart-Allmaras and standard $k$-$\omega$ models predict a primary vortex that is more circular, but have cores of much less strength (suction level) than seen in experiment. Of the eddy viscosity turbulent models the best, in

terms of resolving a primary and secondary vortex that is closest in structure and strength to that measured in experiment, seem to be the $k$–$\varepsilon$ Realizable and RNG turbulence models. Both resolved flow fields have near circular primary vortices with distinct cores of about the right suction level, and with a distinct "tongue" of airflow swept under the primary vortex which has almost a freestream level of total pressure. Of the higher order simulation methods, the Detached Eddy Simulation (DES) and the Scale Adaptive Simulation (SAS) predicted flowfield seems to be the closest to that measured experimentally. The SAS prediction gives a slightly smaller vortex, while the DES prediction slightly larger.

The comparison of the contours of local Mach number at the plane x/D=5, which is plotted in figure 12, confirms that while there is a primary separation, the separated shear layer has not yet fully rolled up to form a vortex at this station. All of the turbulence methods seem to have captured the local Mach number of the flow well enough, with some minor differences between each other and with the experimental contours. Excessive dissipation at the edge of the shear layer is evident in the result from the standard $k$-$\omega$ model, which is consistent with the evidence from the total pressure contours. Further downstream at $x/D = 7$ (figure 13) the local Mach number contours reveal an evolving primary vortex. Of the steady, eddy viscosity models the $k$-$\omega$ SST model and the RNG and Realizable $k$-$\varepsilon$ models appear to provide the closest match with the experimentally measured Mach number contours. The Solution Adaptive Simulation result is the best result from the unsteady simulation methods, but none of the turbulence methods sufficiently resolves the penetration, under the primary vortex, of the flow swept in from the leeside freestream. At the rear measurement station (figure 14) the experimental Mach number contours display a very circular primary vortex structure and a considerable penetration into the shear layer, and roll up, of high speed air induced from the freestream by the vortex. None of the turbulence methods successfully resolve the subtle details of this flow structure, but the closest match appears to be with the two modified $k$-$\varepsilon$ based models and with Solution Adaptive Simulation and Detached Eddy Simulation.

The comparisons for local flow angle are plotted in figures 15 – 17. At $x/D = 5$, presented in figure 15, shows evidence of a small reverse flow region close to the leeside body surface where there is a sheet of what seems to be highly sheared flow (where the flow angle gradient from positive (yellow) to negative (blue) is very pronounced. None of the numerically predicted gradients of the flow angle in this region are captured with the same steepness as seen in the experimental measurement. The Baldwin-Lomax model with the Degani-Schiff modification fails to capture the flow curvature on the windward side of the body that all of the other turbulent methods appear to resolve. In the $x/D = 7$ plane (figure 16), the evolving vortex is now evident in the experimentally measured flow field, much more than is evident in any of the numerical predictions. Again, while the numerical prediction successfully capture the general trends in the flow and generally the right magnitudes of flow angles the agreement between the turbulence methods (apart from the Baldwin-Lomax zero equation method) agree better with themselves that with the experimental measurement in many subtle ways, particularly in the resolution of the detail in the region of the evolving leeside vortex. The agreement between experiment and the CFD solutions appears to be better at station $x/D = 9$ (figure 17). All of the numerical turbulence methods successfully resolve a fully formed leeside primary vortex, albeit with differences in the shape, location and local flow angle in the core. None of the numerical methods agree in the detail of the flow angle distribution in the separated shear layer or, in particular, in the region above the primary vortex. In general all of the turbulence methods, with the exception of the zero-equation B-L model, resolve the core of the primary vortex too close to the windward symmetry plane when compared with the experimental measurement. When comparing the contours of the local flow angle, there does not appear to be any particular "best" turbulence method.
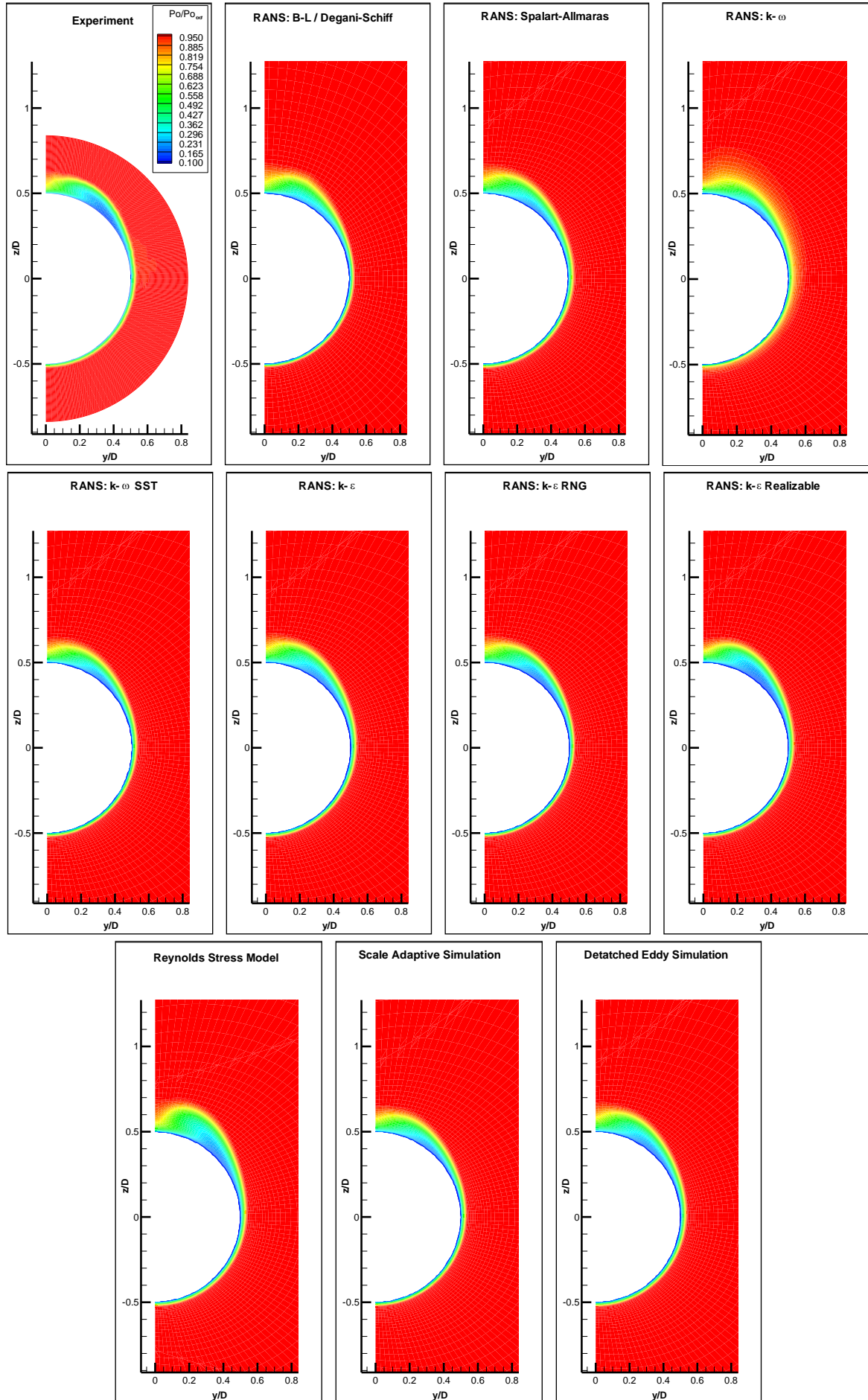
*Figure 9: Comparison of total pressure ratio, B2, $\alpha = 10^o$, M=2.00, $Re_D$=1.2x$10^6$, x/D=5*

24

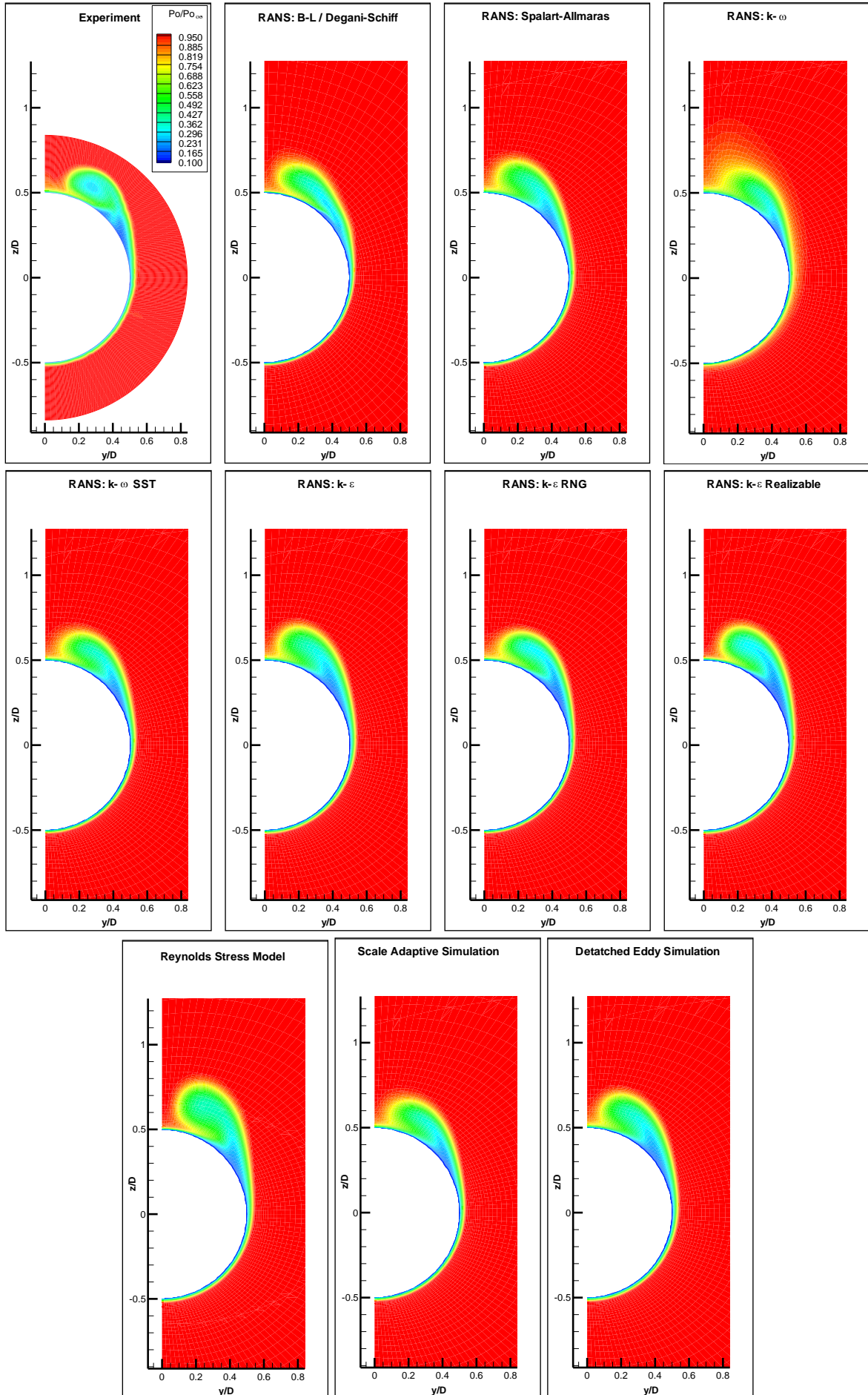*Figure 10: Comparison of total pressure ratio, B2, $\alpha = 10^o$, M=2.00, $Re_D=1.2x10^6$, x/D=7*

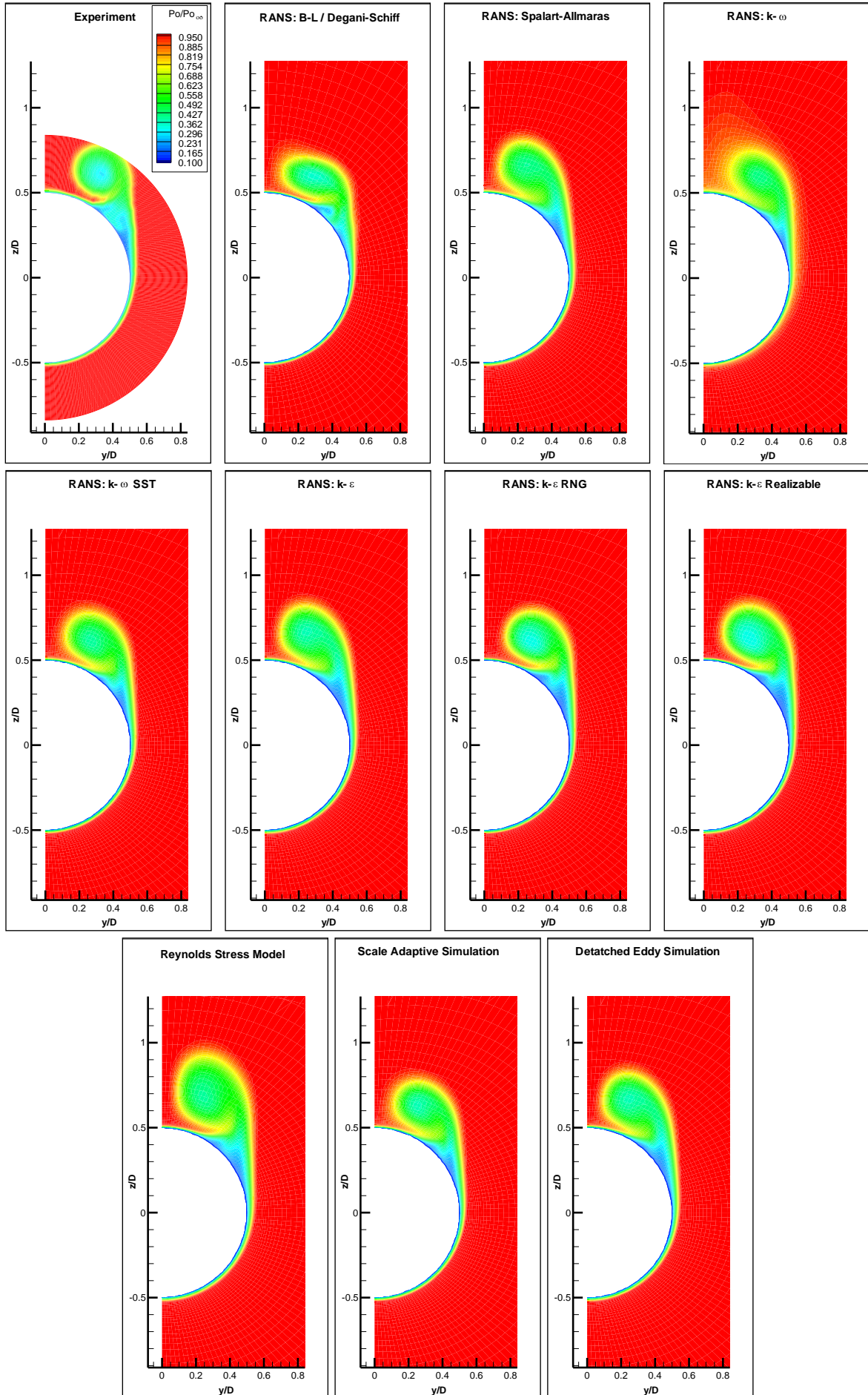*Figure 11: Comparison of total pressure ratio, B2, $\alpha = 10^o$, M=2.00, $Re_D$=1.2x10$^6$, x/D=9*

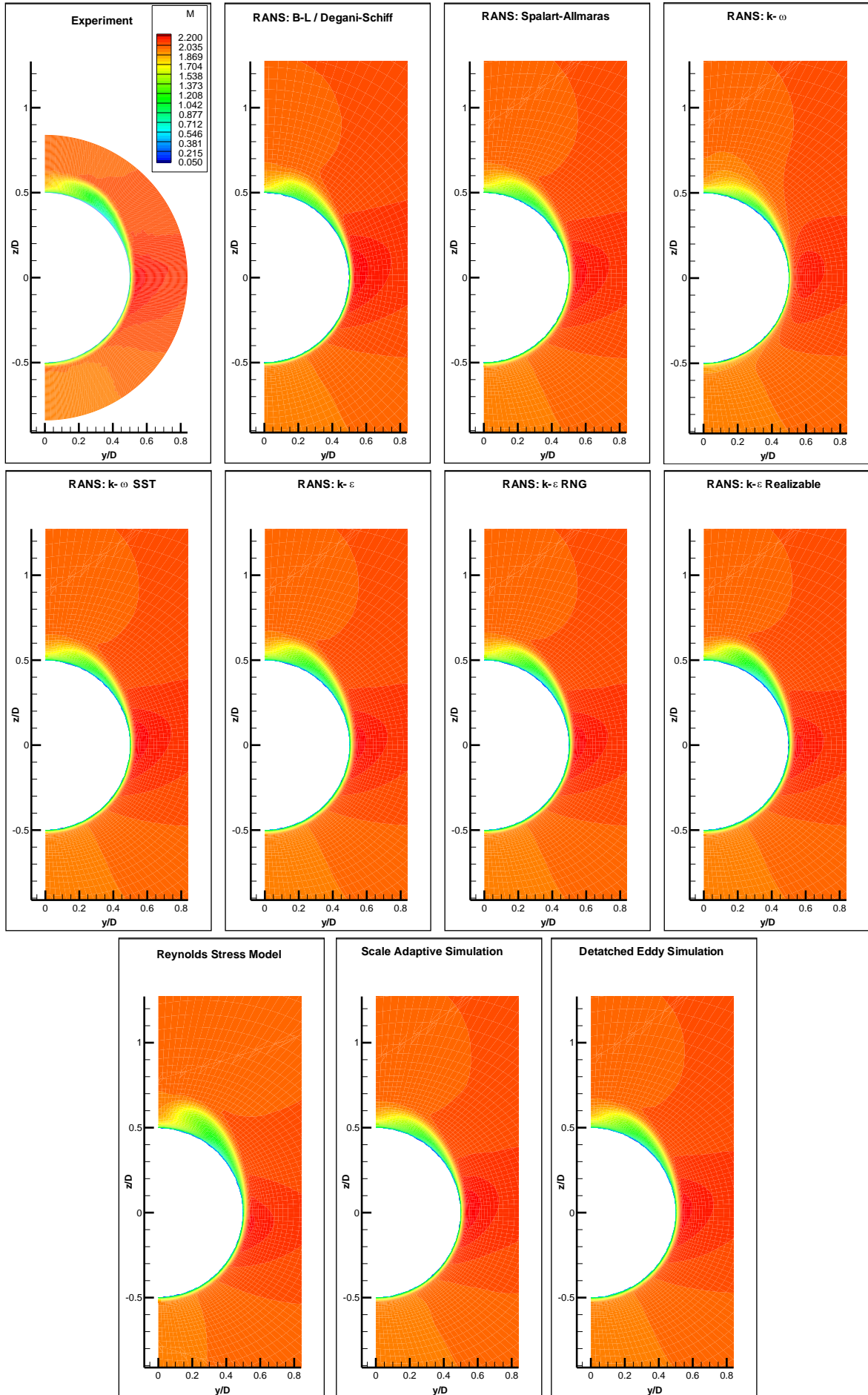*Figure 12: Comparison of local Mach number, B2, α = 10°, M=2.00, Re$_D$=1.2x10$^6$, x/D=5*

27
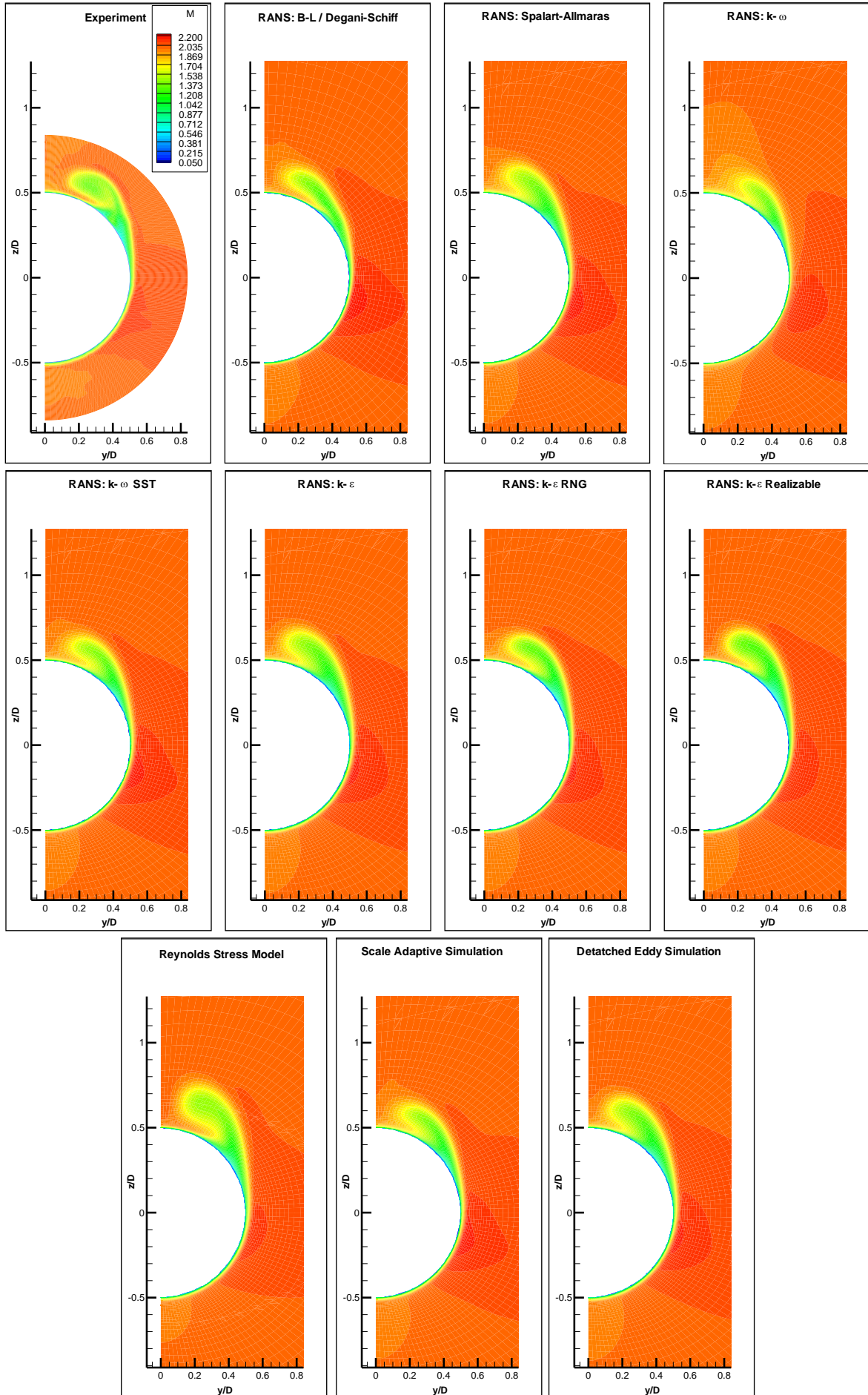
*Figure 13: Comparison of local Mach number, B2, $\alpha = 10^o$, M=2.00, $Re_D=1.2x10^6$, x/D=7*
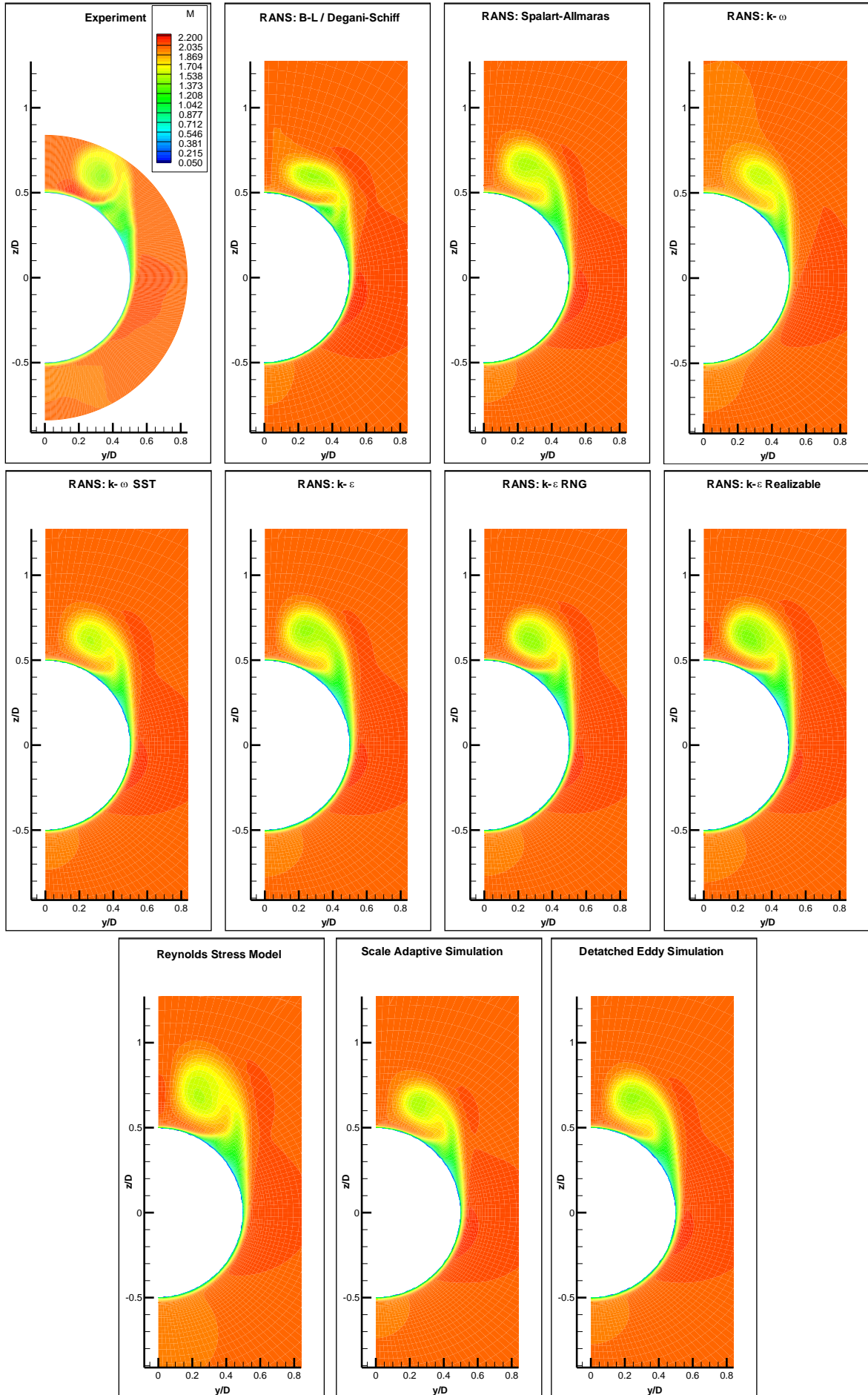
*Figure 14: Comparison of local Mach number, B2, $\alpha = 10^o$, M=2.00, $Re_D=1.2x10^6$, x/D=9*
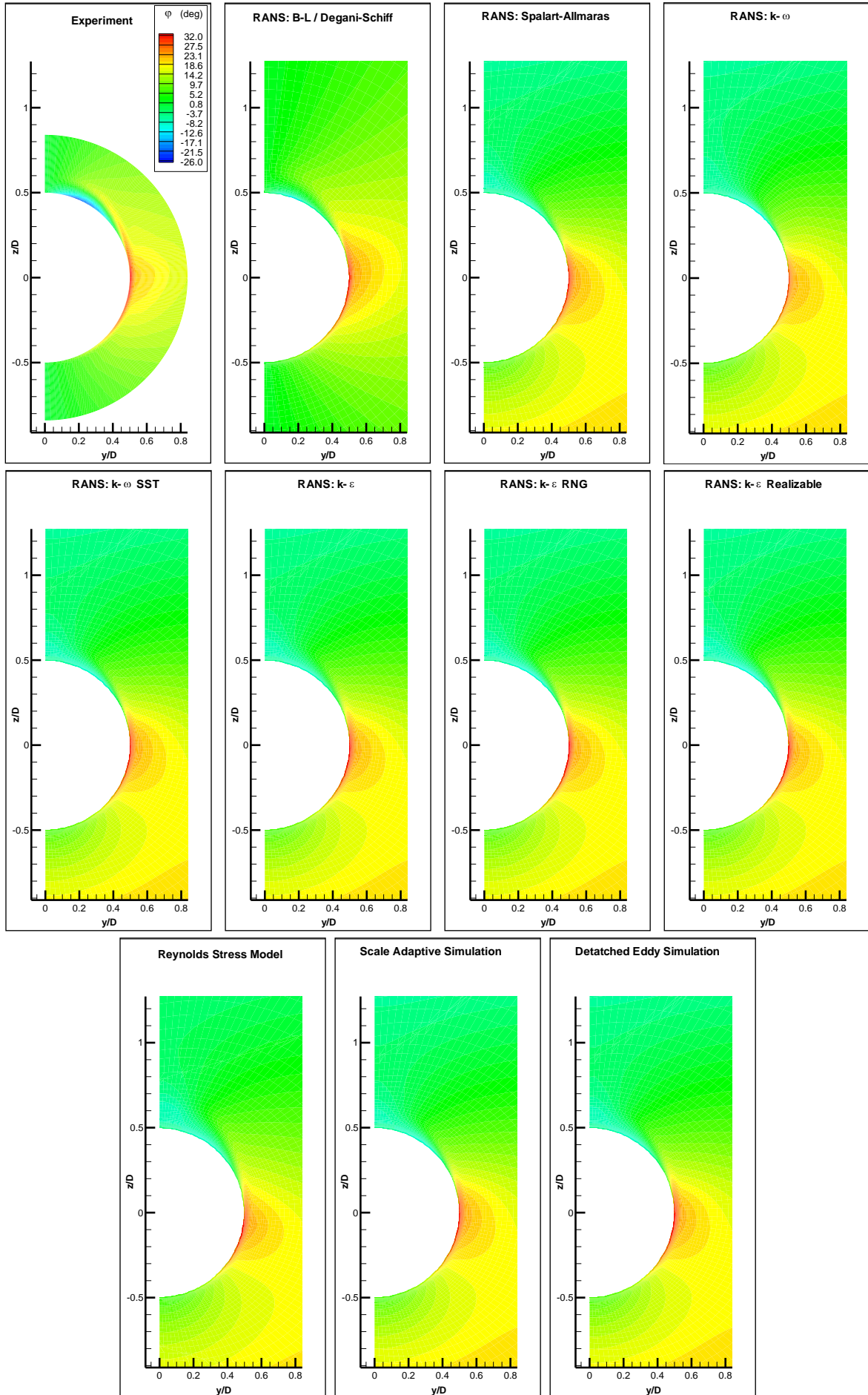
*Figure 15: Comparison of local flow angle, B2, $\alpha = 10^o$, M=2.00, $Re_D=1.2x10^6$, x/D=5*
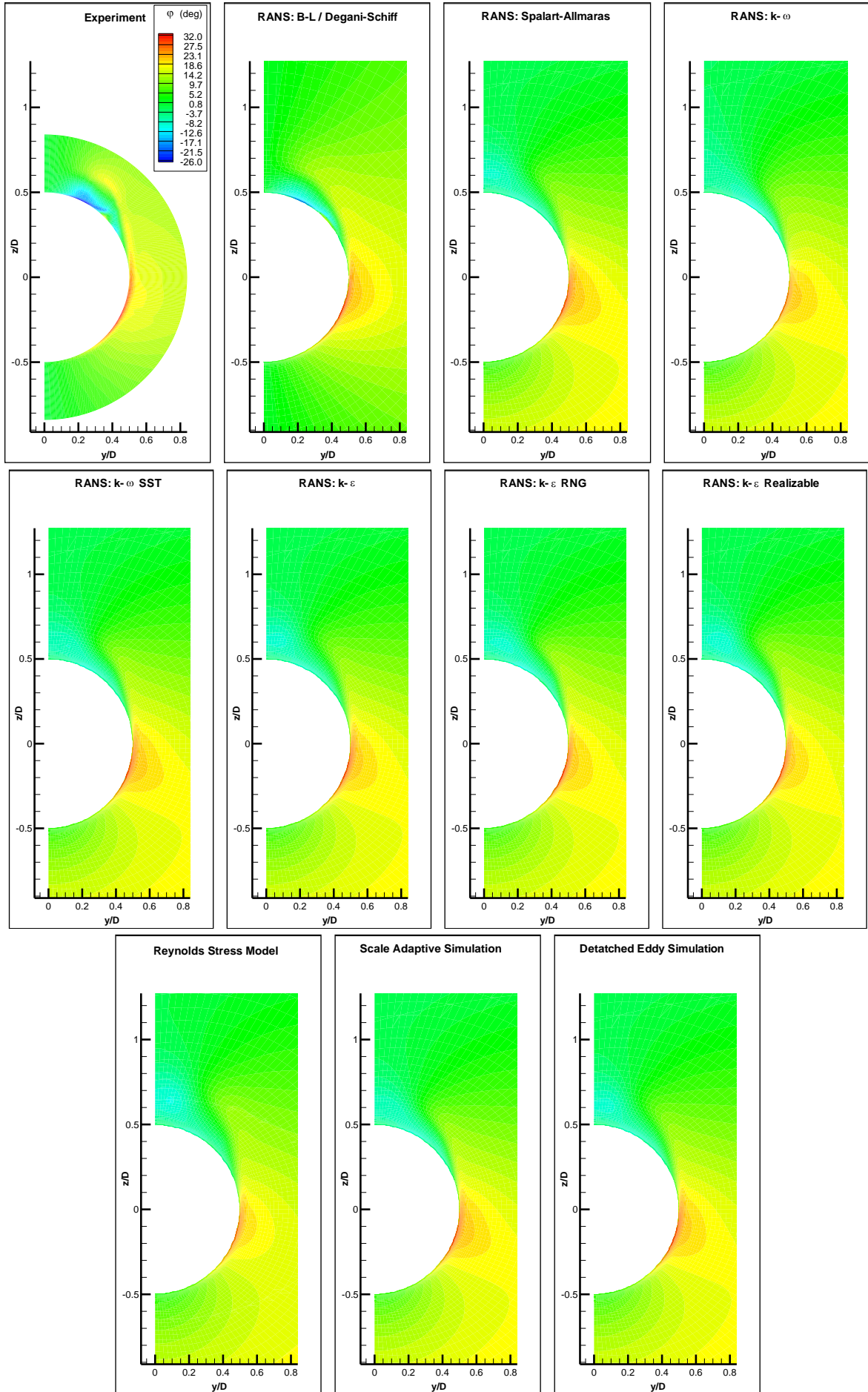
*Figure 16: Comparison of local flow angle, B2, $\alpha = 10^o$, M=2.00, $Re_D=1.2x10^6$, x/D=7*
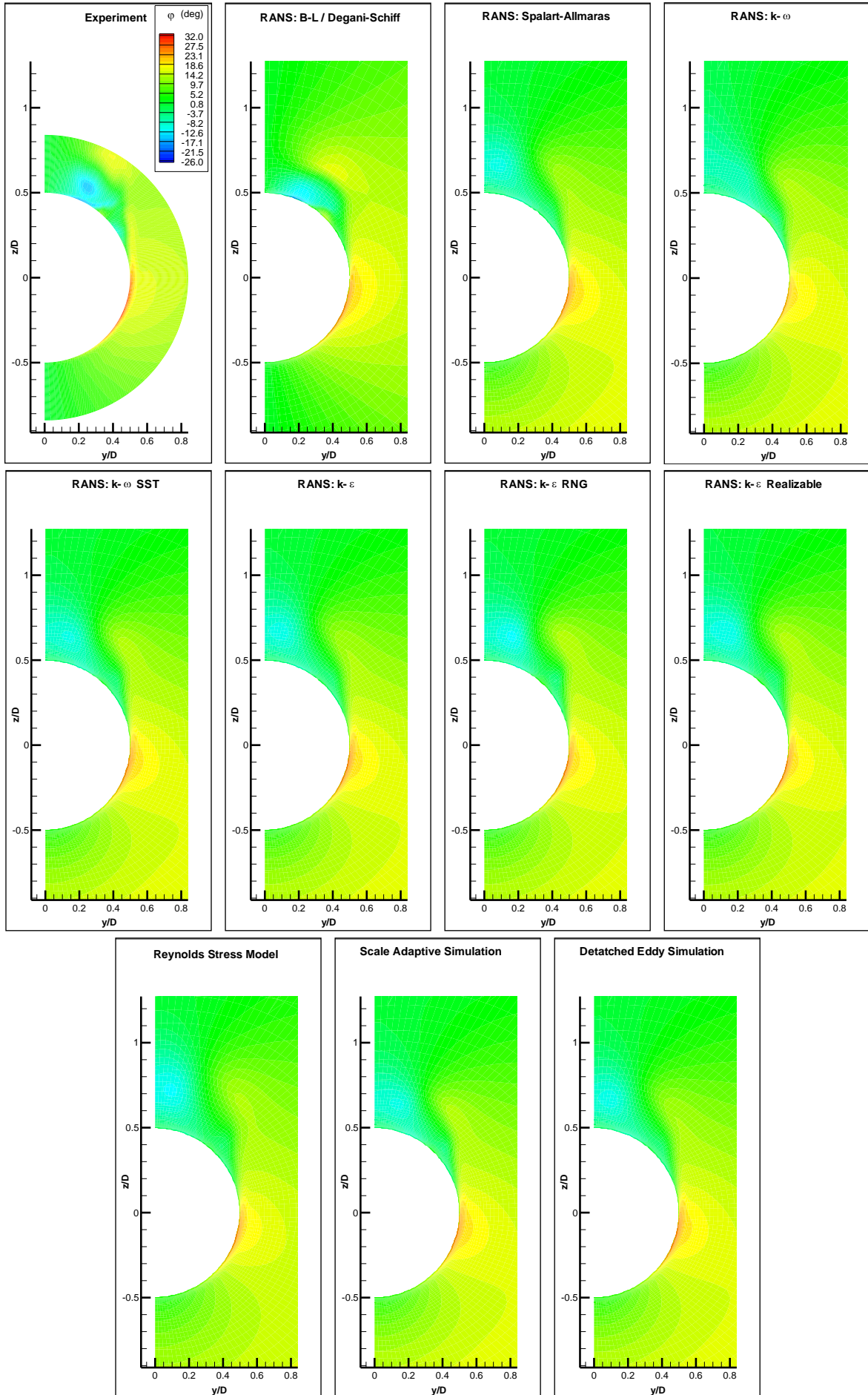
*Figure 17: Comparison of local flow angle, B2, $\alpha = 10^o$, M=2.00, $Re_D=1.2x10^6$, x/D=9*

The comparison between the experimentally measured surface pressure distributions on the body and those obtained by numerical prediction are, perhaps, more informative than the crossflow contour plots because the differences between the methods are more apparent. These comparisons are presented in figure 18, for five axial stations from $x/D = 3$ at the junction of the ogival nose and the cylinder, where the flow begins to over-expand, to $x/D = 12$, and plot the $C_p$ distribution in terms of the circumferential angle, $\phi$, from the windward symmetry plane ($\phi = 0^\circ$) to the leeward symmetry plane ($\phi = 180^\circ$). The left hand plot for each axial station, the RANS turbulence models are compared with the experimental data, while the separate, right hand plot presents the corresponding comparison for the scale resolving methods for improved clarity.

At the first axial station, $x/D = 3$, there is a considerable difference in the magnitude of the measured pressures at a given $\phi$ angle, and those numerically predicted such that it appears that there is a pressure offset. All of the numerically predicted $C_p$ curves are practically identical on the windward surface, and only two causes for this significant discrepancy can be suggested. Either the Navier-Stokes solution has not properly resolved the expanding supersonic flow in this region properly or there is some discrepancy in the published experimental data for this axial station. The excellent agreement between the experimental measured and the CFD resolved surface pressures for the zero angle of attack case, which used exactly the same gird / solution methodology as this case, tends to suggest the latter cause.

Despite this it is clear that all of the Navier-Stokes solutions successfully resolved the correct shape and relative magnitude of $C_p$ at this station, with differences visible in the leeside surface pressures. Neither experiment or CFD pressure curves show any indication of any plateau, indicative of large scale separation, or any leeside vortex suction. At station $x/D = 5$, the agreement between the experimentally measured $C_p$ and the numerically predicted values on the leeside are now, as expected, very good and certainly within the limits of experimental accuracy. On the leeside of the experimental pressure distribution a pronounced inversion and a shallow suction peak is seen, caused by the proximity to the surface of the core of the forming primary vortex, as shown in figure 9. While all of the CFD methods successfully resolved a crossflow separation, and the corresponding inversion in the leeside $C_p$ distribution, none of them were able to resolve the depth of the suction measured in the experiment. The Baldwin-Lomax based solution failed to capture the steepness of the leeside adverse pressure gradient immediately after the flow passes around the shoulder of the body ($\phi = 90^\circ$), while the $k$-$\varepsilon$ Realizable model, failed to capture the magnitude of the peak suction at the shoulder as seen in the experimental measurement, although it performed best in resolving the primary vortex suction. The turbulence methods which provided the best agreement with the experimentally measured data at this station appear to be the $k$-$\omega$ SST turbulence model, and Scale Adaptive Simulation, although the other scale resolving methods provide almost as good a match.

At $x/D = 7$, the experimentally measured $C_p$ curve exhibits a very strong primary vortex suction peak, which has a peak suction almost to the level of that at the body shoulder. There is also evidence of a $C_p$ inversion at $\phi = 135^\circ$, which is associated with a small secondary separation evidenced in figure 9. There is considerable difference between the turbulence methods in the resolution of the peak suction at the shoulder, and that due to the primary leeside vortex. The Baldwin-Lomax / Degani-Schiff model is seen to be the worst at overpredicting the expansion of the flow around the body shoulder, while the $k$-$\varepsilon$ Realizable model is seen to be the worst at underpredicting this expansion. Perhaps the best overall match with the experimental $C_p$ at this station is the $k$-$\varepsilon$ RNG model, but even in this case the level of peak vortex suction, from the plateau level before the peak, is only half that measured in experiment. None of the CFD methods were able to properly resolve the depth of this vortex suction.

The same is not true at the next axial station, $x/D = 9$, where the agreement between the experimentally measured $C_p$ curve and those obtained by numerical calculation are much better. There is still some scatter in the CFD predictions in the regions of the body shoulder and in the primary vortex suction, but the resolution of the peak vortex suction is now much better captured by all methods. Figure 10 shows that at this station, the vortex is now fully formed. The best agreement with experimental data at this station are achieved with the $k$-$\varepsilon$ Realizable and RNG models, and the

scale resolving simulation methods, particularly the Scale Adaptive Simulation method. The Baldwin-Lomax / Degani-Schiff, Spalart-Allmaras and the $k$-$\omega$ models perform the least well here. At the most rearward measurement station, $x/D = 12$, the measured $C_p$ distribution shows that the primary vortex peak has collapsed to a very small level, a phenomenon which is successfully resolved by all of the turbulent Navier-Stokes CFD methods. Scrutiny of the CFD solutions shows that this is due to the leeward convection vortex core away from the body surface, and not due to any vortex breakdown. There is some discrepancy between the CFD resolved $C_p$ curves on the windward body surface and those measured in the experiment, but generally this within the limits of experimental accuracy. There is much closer agreement between all of the numerically predicted $C_p$ curves at this station, but the best agreement with the experimental data is achieved by the same methods that were found to be the best at the previous station.

These surface pressure distributions, both experimentally measured and CFD predicted, can be integrated around the body circumference to provide the axial distribution of the local normal force. These integrated distributions are plotted in figure 19, with the comparison of the RANS turbulence models with experiment plotted on the left and the corresponding comparison for the scale resolving methods plotted on the right-hand side. The result shows that all CFD methods predict the contribution of the nose to the total normal force relatively accurately, though they all agree in underpredicting the experimental peak local normal force by about 10%, though this may be a combination of the accuracy of the experimental pressure measurements and the numerical integration method used. On the afterbody there is seen to be considerable differences in the resolution of the local normal force contribution between the different CFD turbulence methods. The Spalart-Allmaras model appears to underpredict the local $C_N$ the most, while the $k$-$\varepsilon$ Realizable and RNG turbulence models give curves that pass very much through the experimental data, and actually outperform the scale resolving methods.

The comparison of the experimentally measured, and computationally predicted normal force and axial force coefficients are presented in figure 20, as bar charts. The experimental figure is plotted as a green bar with the result extended across as a straight line for comparison with the data for the computational methods. For the normal force coefficient, all of the CFD turbulence methods except the standard $k$-$\omega$ turbulence model underpredict the measured normal force. All of the methods give predicted $C_N$ to within 15% of the measured value, with the most accurate result generated using the $k$-$\varepsilon$ Realizable turbulence model which gave a result only 3% below the experimental value. For the axial force coefficient comparison, similarly plotted, all of the CFD turbulence methods overpredicted the experimentally measured result. Given that this parameter is usually the most challenging to predict, since a significant proportion of the force is derived from surface skin friction, the fact that all but the standard $k$-$\varepsilon$ turbulence model predict this to within 8% of the measured value, which itself has an accuracy of 5%, is an impressive result. Paradoxically, the best prediction comes from the method with the least physical modelling fidelity – the Baldwin-Lomax zero equation method. This is almost certainly a fluke. The next best comparisons come from the $k$-$\omega$ SST turbulence model, and the Scale Adaptive Simulation and Detached Eddy Simulation methods, which predict $C_A$ to within 5% of the experimental result.
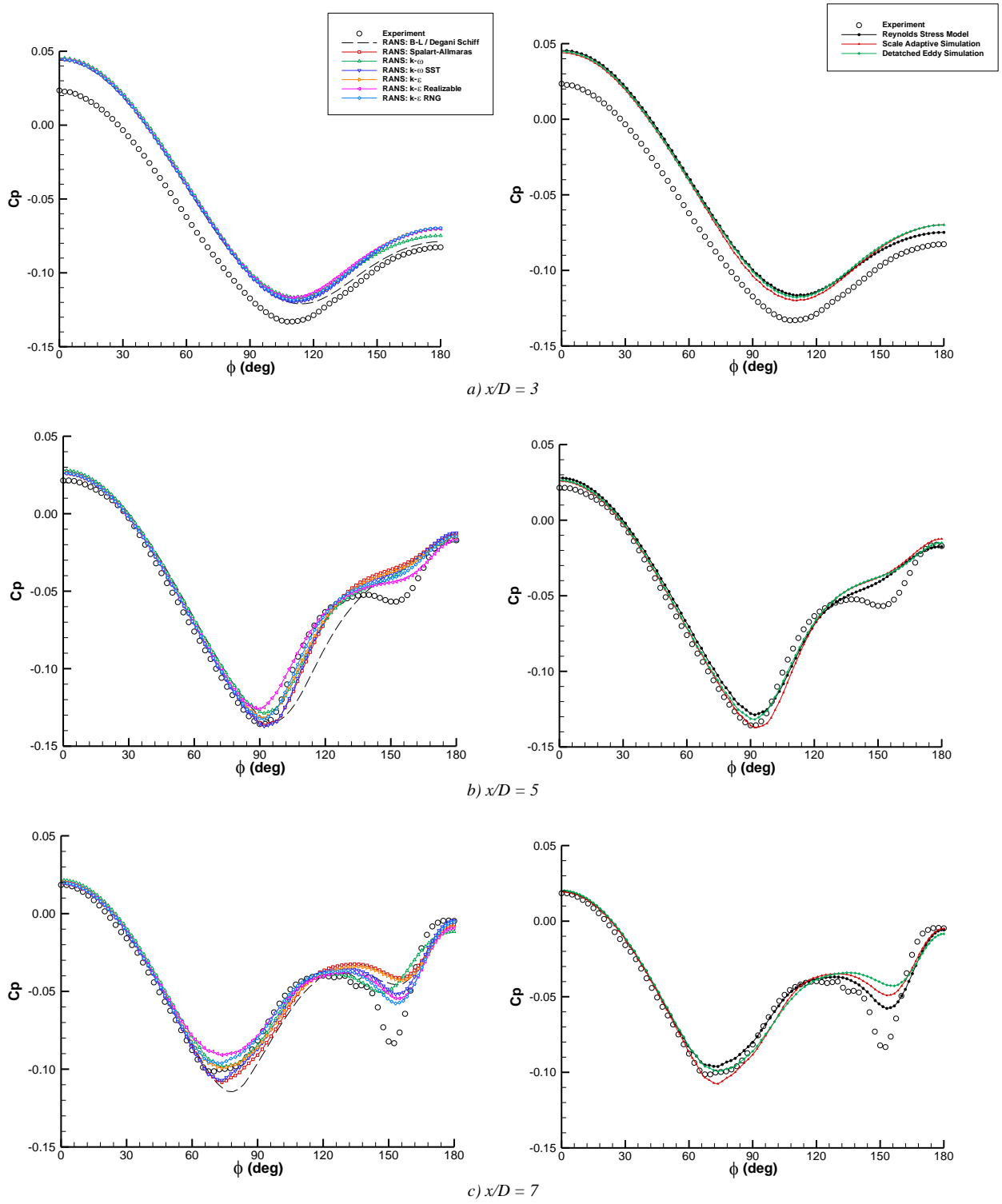
*Figure 18: Comparison of circumferential surface Cp distribution, B2, α = 10º, M=2.0, Re$_D$=1.2x10$^6$. RANS predictions (left), and scale resolving predictions (right).*

*d) x/D = 9*



*e) x/D = 12*

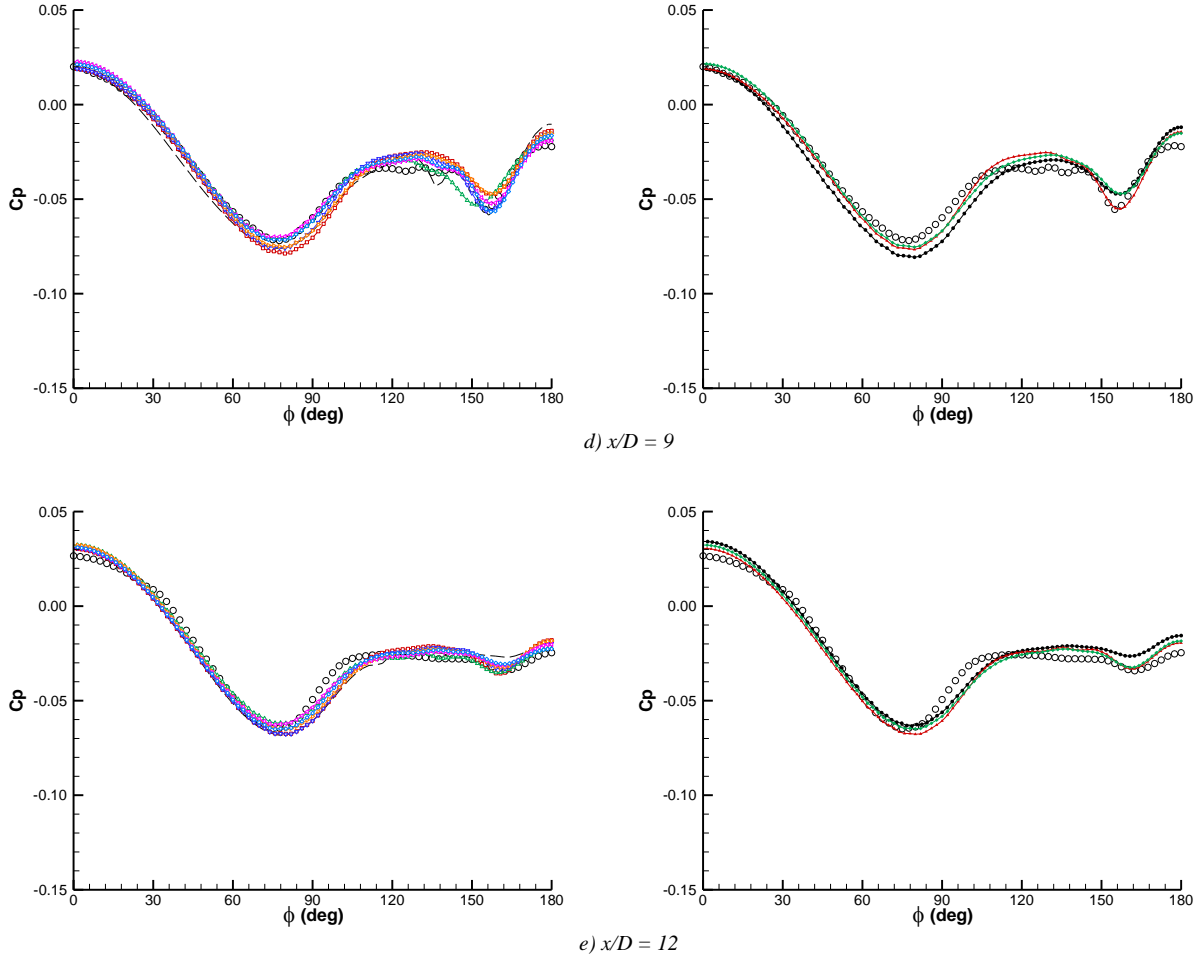*Figure 18: Comparison of circumferential surface Cp distribution, B2, $\alpha = 10^o$, M=2.0, $Re_D=1.2x10^6$ (concluded). RANS predictions (left), and scale resolving predictions (right).*
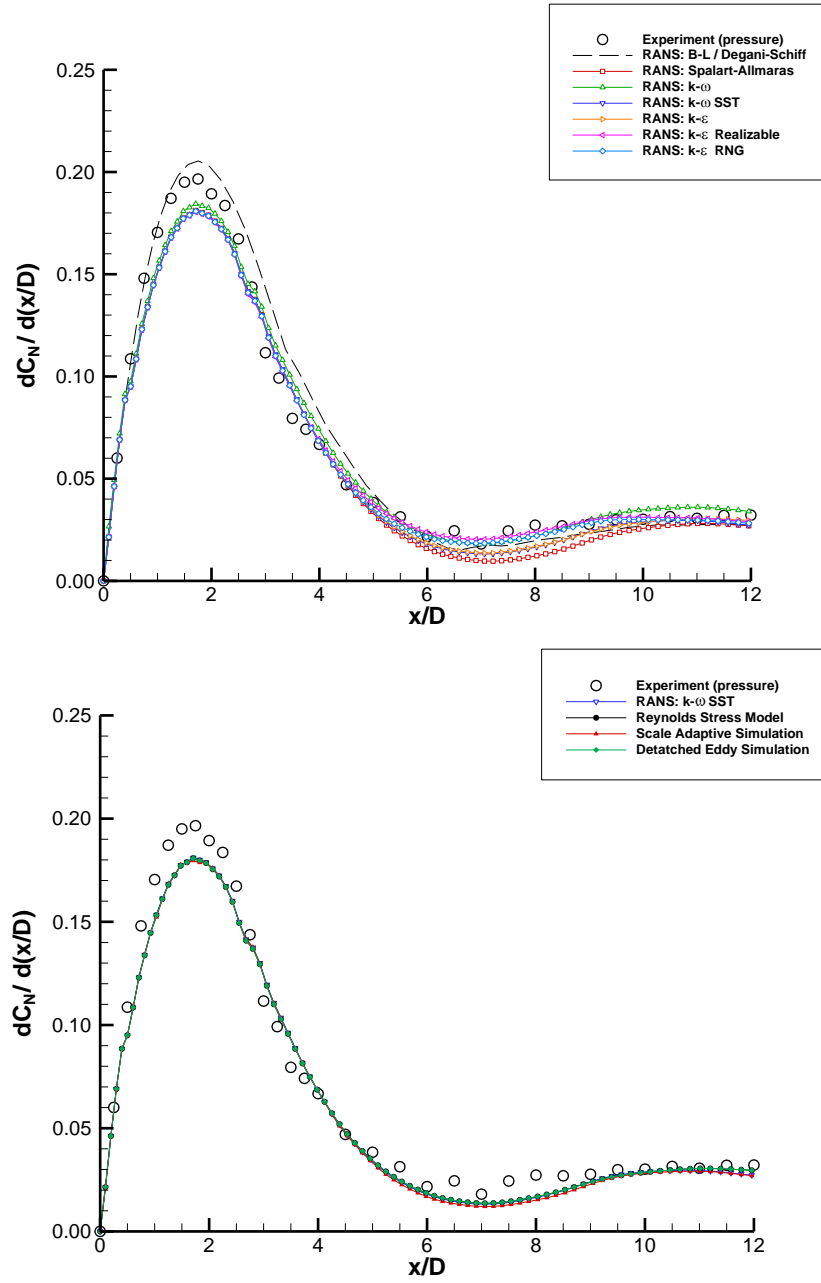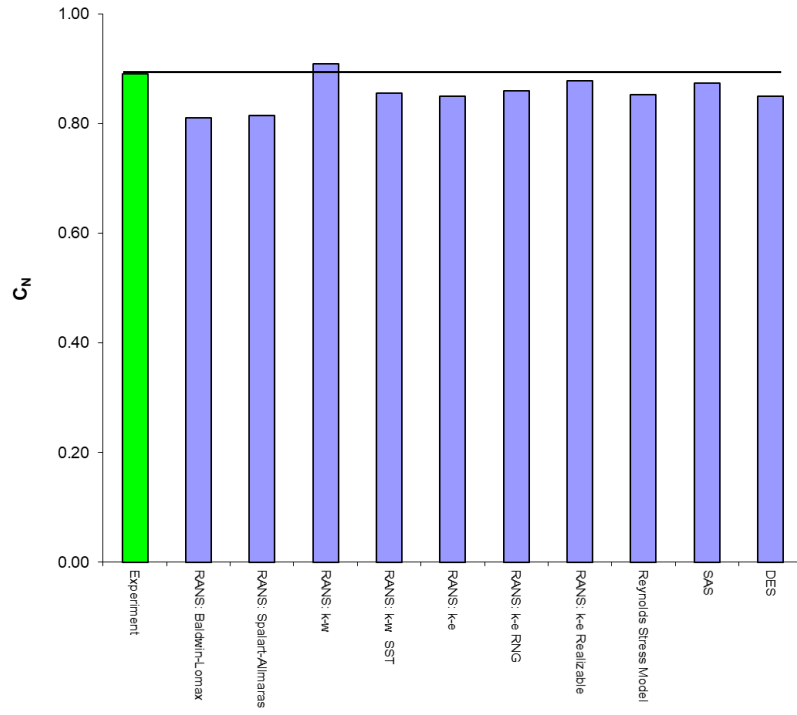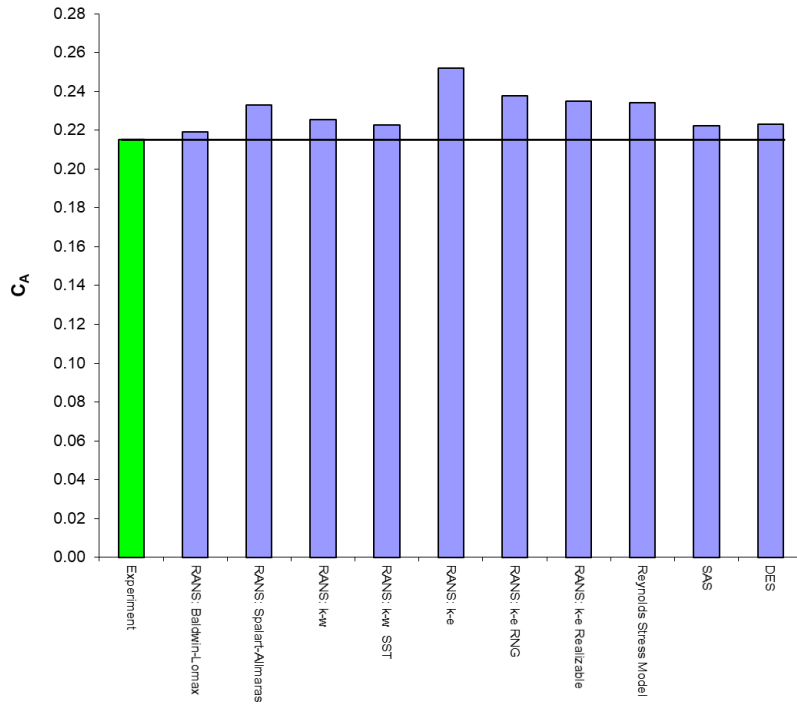
*Figure 19: Comparison of local normal force distribution, B2, $\alpha = 10^o$, M=2.0, $Re_D$=1.2x10$^6$. RANS predictions (left), and scale resolving predictions (right).*

*a)   Normal force coefficient, $C_N$.*



*b)   Axial force coefficient, $C_A$.*

*Figure 20: Comparison of measured and predicted force and moment characteristics, B2, $\alpha = 10^o$, M=2.0, $Re_D=1.2x10^6$.*

## 4.3   B1A, M=0.7, $\alpha = 14^o$ Test Case

For this subsonic Mach 0.7 B1A body case the CFD results are compared with the corresponding experimental measurements in figures 21 -23. Here the same grid sensitivity assessment was performed as with the B2 studies presented in sections 4.1 and 4.2, to ensure mesh independent results. Figure 21 presents the comparison at a crossflow plane at $x/D = 8.5$ of the total pressure ratio contours, between the experimentally measured data, in the top left corner, and the results obtained with the turbulent Navier-Stokes methods. What is noticed is that the experimental pitot measurements were acquired only in the leeward sector of the flow field from $\phi = 120^o$ to the leeward symmetry plane, focussing on resolving the leeside vortical flow features. Also, it is seen that the pitot measurements do not extend all the way to the surface of the body, which is denoted by the black circular line to aid in interpreting the data. The vortex at this axial station is seen to be fully developed with a well defined central core of low pressure air and a distinct "tongue" of freestream air swept in under it. While all of the computational methods are seen to have successfully resolved a strong leeside primary vortex, not all of them provide accurate vortex structure, size, position and strength. The worst prediction, in comparison with the experimental flow field, is seen to be that obtained using the standard $k$-$\varepsilon$ turbulence model which predicts a vortex that is too large and elongated, with no distinct core and appears too dissipated. The Baldwin-Lomax model with the Degani-Schiff modification predicts a vortex which is slightly too small in height, whose vortex core has a pressure of too low magnitude and has no tongue of freestream air induced under it. The other methods are more successful in predicting the primary vortex characteristics, with distinct cores and much better shape and position. The best overall prediction would seem to be obtained using one of the simulation methods, whose predictions are very similar, or the Spalart-Allmaras, $k$-$\omega$ SST or $k$-$\varepsilon$ Realizable turbulence models, which also resolve the tongue of freestream air swept under the primary vortex and the core location and suction magnitude to a reasonable level.

These findings are reproduced in the corresponding comparisons for the axial station $x/D = $ 11.5, presented in figure 22. Here the measured primary vortex is seen to have grown more elliptic in shape as it has evolved downstream, but still retains a distinct core of low pressure air. The same conclusions can be derived here as were stated for the previous axial station, though the predictions which best match the experimental contours here are those obtained using the Spalart-Allmaras and $k$-$\omega$ SST turbulence models, and Detached Eddy Simulation, which best capture the extent of the "tongue" and the associated magnitude of the total pressure underneath the vortex. The other simulation methods and the $k$-$\varepsilon$ Realizable turbulence model appear to give predictions that are almost as accurate against the experimental measurement.

The experimentally measured and numerically predicted surface pressure distributions are compared in figure 23 for five axial stations from $x/D$=3.5 to 11.5 in the same way as in figure 18 for the B2 supersonic case. Across all of the axial stations, the peak suction at the shoulder of the body is well resolved by all of the methods except the Baldwin-Lomax based zero-equation model, which significantly overpredicts the suction. The significant differences between the turbulence methods are in the resolution of the pressure distribution over the leeside of the body.

The measured surface pressure distribution at $x/D = 3.5$ exhibits an inflexion at around $\phi = 140^o$ which is due to a crossflow separation, which forms a separation bubble prior to it breaking down to form a streamwise vortex further downstream. All of the turbulent CFD methods successfully resolve this feature to some degree of accuracy. The peak suction at the shoulder of the body is well resolved by all of the methods except the Baldwin-Lomax based model. All of the other methods slightly underpredict this suction, with all but the result of the $k$-$\varepsilon$ model being within the limits of experimental accuracy. The $k$-$\varepsilon$ RNG turbulence model underpredicts the suction on the windward body side the most, but there is little difference between the other turbulence models until the flow reaches the leeside. Here the standard $k$-$\omega$ model appears to predict the emerging secondary suction peak due to the forming primary vortex. Overall the most accurate prediction at this axial station

comes from Detached Eddy Simulation, but the other simulation methods provide $Cp$ distributions that are almost as good.

At the next axial station along, $x/D = 5.5$, the experimental data reveals very strong primary vortex suction around $\phi = 160^o$ which, like the similar case for the B2 body is not well resolved by any of the CFD methods. It seems that the early smooth surface separation and early evolution of the primary leeside vortex is not well captured by any of the CFD methods, even those scale resolving simulation methods that involve the most physical fidelity. It is clear that the Baldwin-Lomax / Degani-Schiff turbulence model performs poorly here, and this is the case for all of the axial stations compared for this subsonic test flow. Of the RANS turbulence models, only the standard $k$-$\varepsilon$ model fails to resolve any primary vortex suction. Surprisingly, perhaps, the standard $k$-$\omega$ model predicts the strongest primary vortex suction, closest to the experimental measurements, but the match with experiment is not as good elsewhere on the leeward side. The Spalart-Allmaras, $k$-$\omega$ SST and $k$-$\varepsilon$ Realizable also successfully resolve strong suction peaks at this station but these are far weaker than that measured in experiment. The solutions obtained by the higher fidelity simulation methods were not much better, capturing a suction of about half the strength measured in experiment.

A similar finding is seen in the results at $x/D = 7.5$, where the experimentally measured vortex suction is much reduced, as the primary vortex convects upwards away from the surface. All of the tested turbulence methods fail to capture the magnitude of suction in the plateau region prior to the vortex suction. Of the turbulence models, the Spalart-Allmaras, $k$-$\omega$ SST and $k$-$\varepsilon$ Realizable models capture the primary vortex suction most accurately. The standard $k$-$\omega$ model now significantly overpredicts this suction. Again, overall, the scale resolving simulation methods capture the $Cp$ distribution marginally better.

While all of the turbulence methods perform better further downstream, at stations $x/D = 9.5$ and 11.5, as the vortex suction diminishes and the pressure plateaus out, the same turbulence methods appear to give the best match with experiment – the scale resolving simulation methods and the Spalart-Allmaras, $k$-$\omega$ SST and $k$-$\varepsilon$ Realizable models, which seem to be consistently the best for this smooth surface separation subsonic flow.
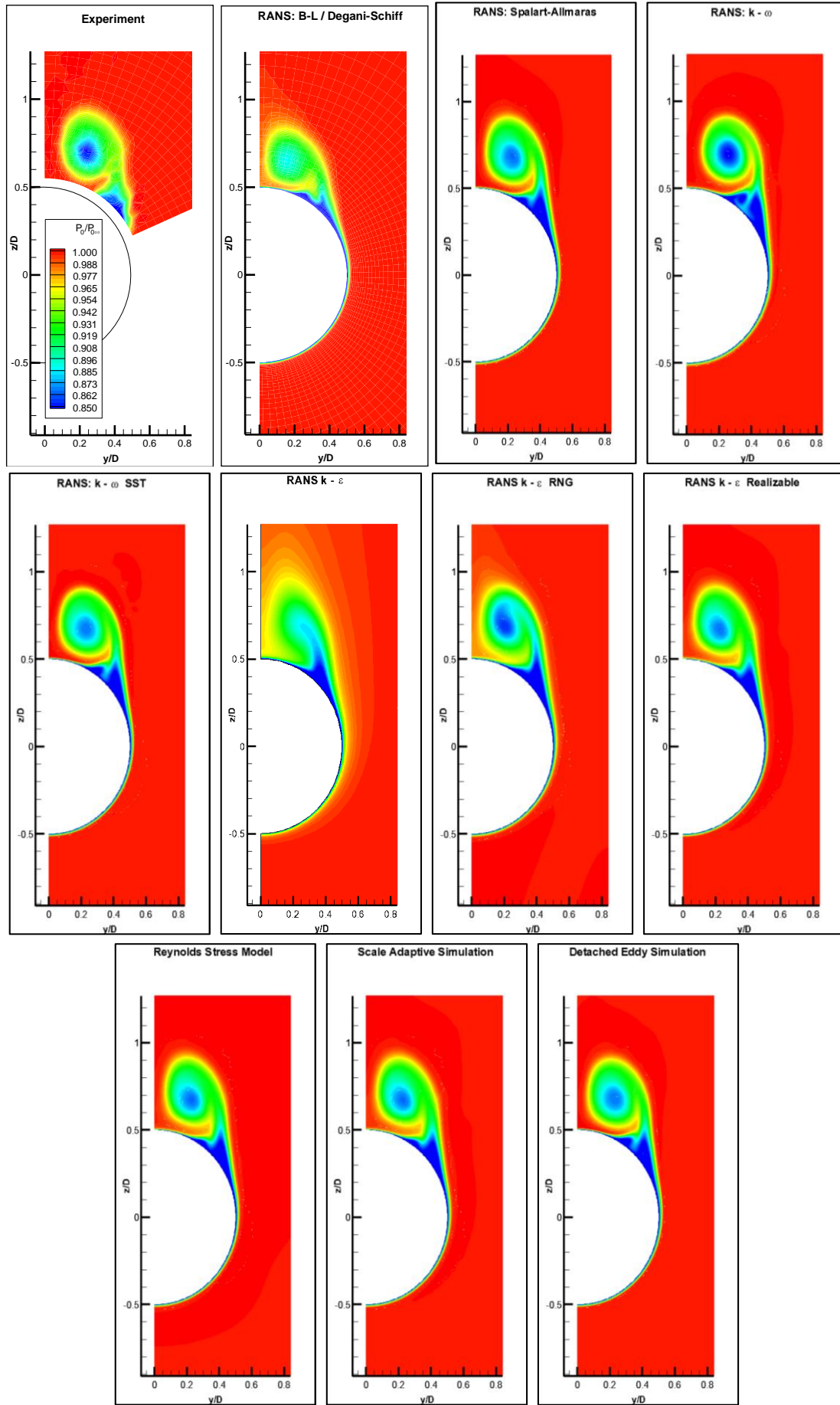
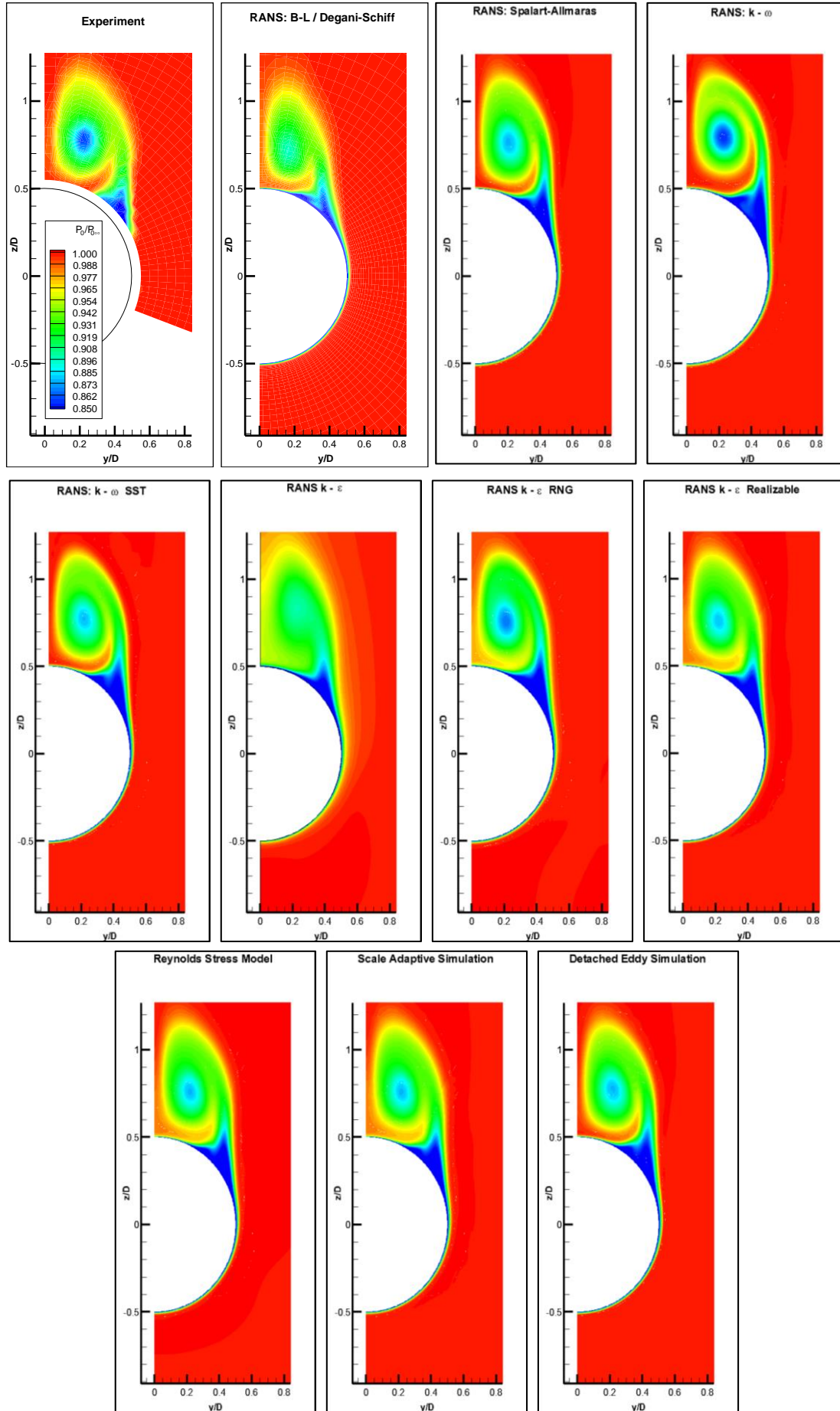*Figure 21: Comparison of total pressure ratio, B1A, $\alpha = 14^o$, M=0.7, $Re_D=0.67x10^6$, x/D=8.5*

*Figure 22: Comparison of total pressure ratio, B1A, $\alpha = 14^o$, M=0.7, $Re_D=0.67 \times 10^6$, x/D=11.5*
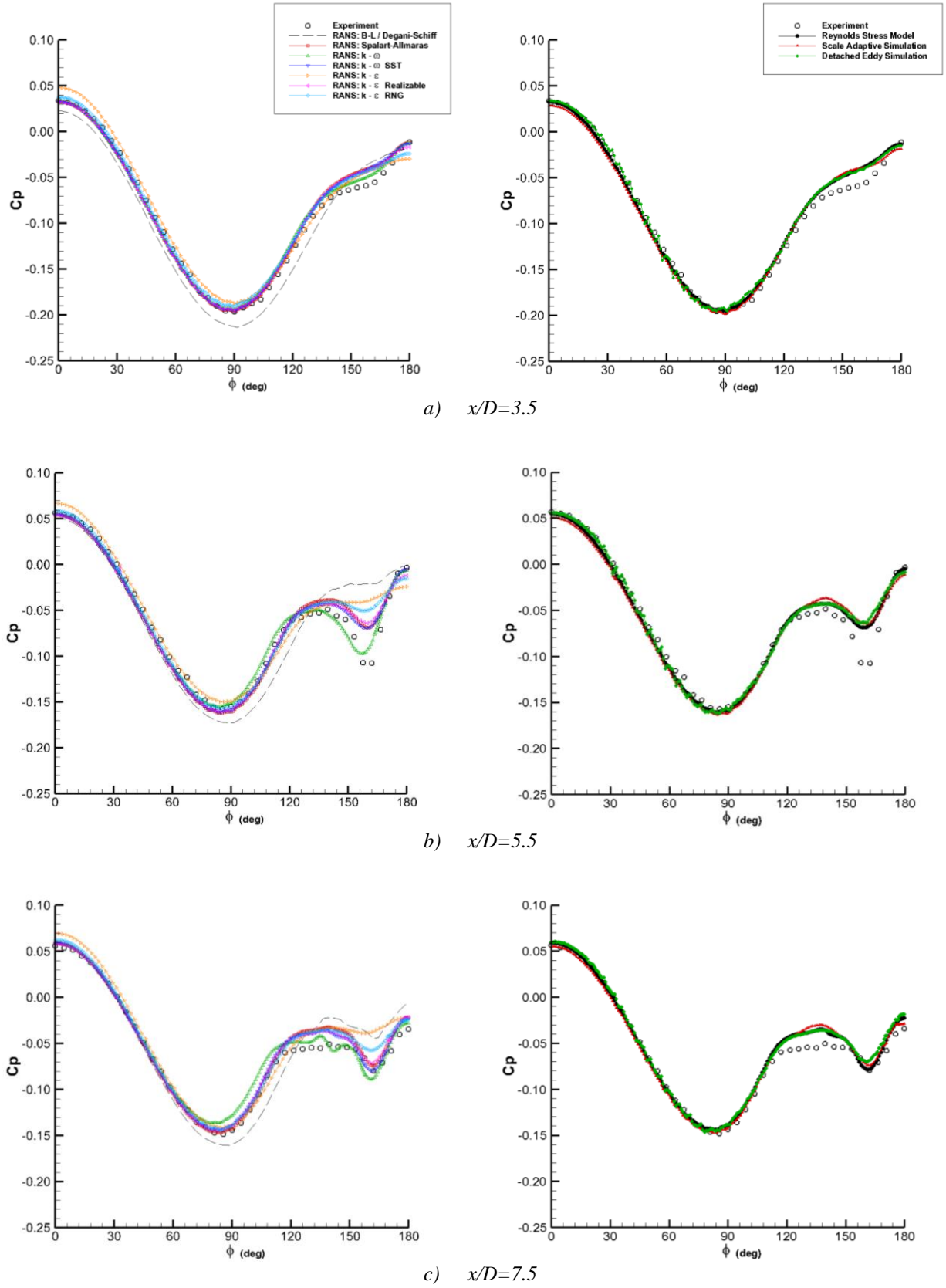
*a)    x/D=3.5*



*b)    x/D=5.5*



*c)    x/D=7.5*

*Figure 23: Comparison of circumferential surface Cp distribution, B1A, $\alpha = 14^o$, M=0.7, $Re_D=0.67x10^6$. RANS predictions (left), and scale resolving predictions (right).*
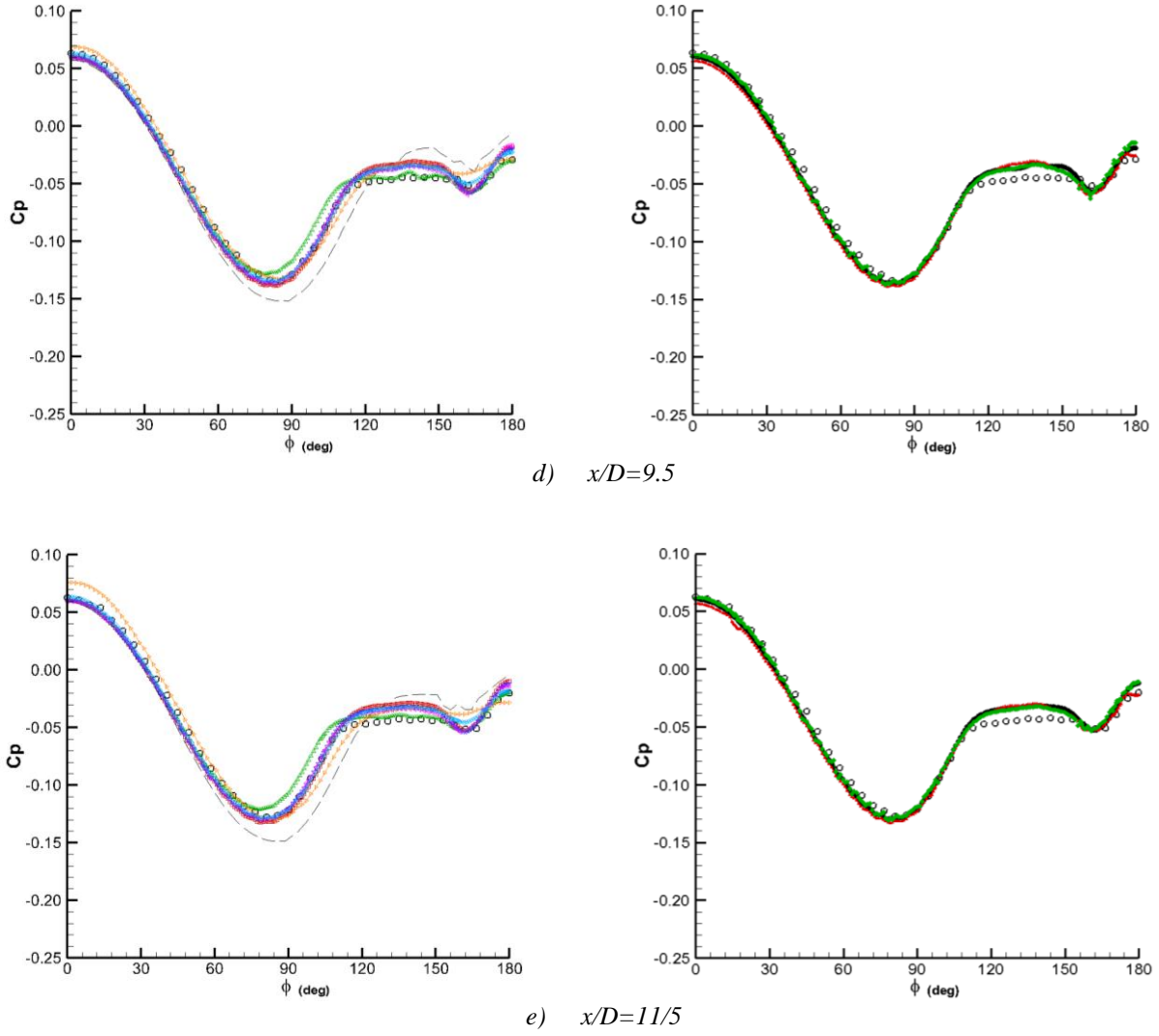
*d)    x/D=9.5*



*e)    x/D=11/5*

*Figure 23: Comparison of circumferential surface Cp distribution, B1A, $\alpha = 14^o$, M=0.7, $Re_D$=0.67x10$^6$ (concluded). RANS predictions (left), and scale resolving predictions (right).*

## 4.4   B1A, M=2.5, $\alpha = 14^o$ Test Case

The freestream flow for this case is supersonic, at Mach 2.5, and so, as with test cases 1 and 2, there will be a conical nose shockwave. This flow is very similar to that seen in test case 2, in that both are at significant angle of attack to the supersonic stream – in this case at a higher 14$^o$ angle of attack. The turbulent boundary layer separates from the smooth cylindrical surface to form a symmetric leeside vortex flow. The difference is that in this case a separate shock wave forms because of the displacement of the streamwise supersonic flow, inside the conical nose shock wave, by the presence of the leeside separated flow. This weaker streamwise conical shock wave appears in the crossflow plane as an embedded crossflow shock wave that is relatively strong in the vicinity of the body, and weakens as it propagates into the freestream. This is clearly evident in the comparisons of the pitot pressure ratio contours plotted for stations *x/D* = 5.5 and 11.5 in figures 24 and 25 respectively. In fact, at both of these stations this shock wave is seen to be strong enough to fix primary boundary layer separation.

At station 5.5 the experimental measurement, which does not extend all the way down to the body surface, resolves the top edge of the primary vortex, and the embedded shock wave emanating from the surface at an angle of about 50$^o$ to the *y*-axis. All of the computational turbulence methods

44

successfully resolve the appearance of the primary vortex in broadly the correct location, but differ in the resolution of the vortex structure. They also correctly resolve the existence of the embedded shock, revealing that its origin, close to the body surface, is the location of boundary layer separation. They also correctly resolve its shape, but not necessarily its strength. The zero equation Baldwin-Lomax / Degani-Schiff turbulence model does a remarkably good job in resolving the embedded shock wave, but the primary vortex is captured further inboard, closer to the leeside symmetry plane, than is indicated in the experimental measurement. The $k$-$\omega$ turbulence model also predicts a primary vortex too inboard, but also resolves a much weaker embedded shock feature that fails to match the strength of that measured in experiment. The vortex predicted using the Spalart-Allmaras model is, perhaps, slightly larger than that measured in experiment, as is that obtained with the standard $k$-$\varepsilon$ model, while the other turbulence models provide much better predictions of both the primary vortex and its associated embedded shock.

While the Reynolds Stress Model and Solution Adaptive Simulation provide a good prediction of the primary vortex, the embedded shock strength appears weaker than seen in the experiment, or in the solutions from the best RANS turbulence models, and appear inferior to the result obtained using Detached Eddy Simulation at this axial station.

At station $x/D = 11.5$, plotted in figure 25, the primary vortex is seen to have grown considerably, and convected further leeward, away from the body. The experimental measurement does not display any evidence of an embedded shock wave, but all of the computational predictions, except that obtained with the standard $k$-$\omega$ model, agree in showing that this shock exists further leeward, outside the region where the measurements were taken. In fact the computational evidence suggests that this embedded shock is still strong enough at this downstream station to fix primary separation, though they disagree on the resolution of its strength. All of the computation predictions successfully captured the larger primary vortex, although the standard $k$-$\omega$ model resolves an unphysically distorted vortex that does not resemble that measured in the experiment. The other turbulence methods resolve a broadly accurate vortex in terms of shape, location and size, but differ in the resolution of the core strength. The best matches with experiment, in terms of the vortex resolution, are achieved with the $k$-$\varepsilon$ Realizable and RNG models, and with Solution Adaptive Simulation, although these disagree in the resolution of the embedded shock strength. Without experimental total pressure measurement data that reveals this shock, however, it is impossible from this data to say which method is best.

A better comparative analysis can, perhaps, be made by scrutiny of the surface pressure measurements and predictions. Figure 26 presents the comparison of the experimentally measured and computationally resolved surface $C_p$ distributions at five axial stations on the body. Here, the comparisons for the RANS turbulence models are plotted on the left, separately to those for the higher fidelity simulation methods which are plotted, for improved clarity, on the right. What is immediately clear from this figure is that the standard $k$-$\omega$ turbulence model fails to resolve the correct surface pressure on the windward side of the body, whereas the corresponding pressures for all other methods agree very well, and are much closer to the experimentally measure surface pressures. This, and all of the other discrepancies seen with this turbulence model, may well be associated with the initial prescription of $\omega$ on the farstream boundaries, which is a known problem with this turbulence model. Without a-priori knowledge of this property, it is difficult to see how this model can be safely used for this application. The other turbulence methods differ in the resolution of the position and strength of the embedded shock, which is observed as the sudden jump in $C_p$ following the smooth windward trend in surface suction. They also differ in the resolution of the subsequent primary and secondary vortex suctions. At $x/D$=3.5, the embedded shock wave is seen to be very weak, and here all of the methods do a good job in resolving, within the limits of the experimental accuracy, the pressure recovery under the evolving primary vortex. Further downstream at $x/D$=5.5 the embedded shock wave is much stronger, resulting in a pressure plateau and a strong primary vortex suction which results in a suction level even stronger than the peak seen before the shock wave. All of the turbulence methods broadly resolve the same $C_p$ trends, but the Baldwin-Lomax based model and the $k$-$\varepsilon$ Realizable model both predict an embedded shock too leeward of that measured in experiment, and

primary vortex suction that is too weak. Of the RANS turbulence models, the best results at this station were provided by the $k$-$\varepsilon$ RNG model and the $k$-$\omega$ SST model, while the best of the higher order methods was Solution Adaptive Simulation.

At $x/D$=7.5 all of the turbulence methods overpredict primary vortex suction, and also resolve a strong inboard secondary vortex suction that does not appear in the experimental measurement. The Reynolds Stress Model result appears particularly poor in the resolution of the vortex suctions, which may be a result of the time averaging used to provide this result, whereby the time sample may not have been long enough. The time sampling for all of the time accurate simulation methods were identical, however. There does not appear to be a clear "best" of the RANS turbulence models, since one may provide a better prediction of the location and strength of the embedded shock, but over predict the vortex suctions, while another gives better prediction of the vortex suctions, but resolves the shock wave poorer. Overall the Solution Adaptive Simulation technique provides the best prediction of all the methods, with a reasonably accurate prediction of the embedded shock pressure, and the closest match with the pressure plateau and weak primary suction peak seen in the experimental measurements.

Much the same can be said of the surface $C_p$ predictions at downstream stations x/D = 9.5 and 11.5, where the experimental measurements show that the effect of the primary vortex, which has convected into the leeside flow away from the body surface, is minimal and a pressure plateau exists from $\phi$ = 90$^{\text{o}}$ to 180$^{\text{o}}$. The most accurate prediction of all the methods is provided by Solution Adaptive Simulation.

Force balance measurements were taken for this test case, and comparisons of the converged forces and moments for the RANS predictions, and of the time averaged forces and moments for the higher order time accurate simulations, can be made. Figure 27 presents the bar chart comparisons for normal force, axial force and pitching moment (about the nose) coefficients together with the axial centre of pressure location. Again the left hand green column shows the experimentally measured value with a corresponding line extending along the plot for ease of comparison. For the normal force coefficient, $C_N$, the two best predictions are from the Baldwin-Lomax / Degani-Schiff model, and the Solution Adaptive Simulation method, both of which predict a figure within 2-3% of the experimental value. For the case of the Balwin-Lomax based model this is probably more of a fluke, as the comparisons for surface pressure and vortex and shock flow structure are not consistently good, as is the case with the Solution Adaptive simulations. The result from the $k$-$\omega$ SST, $k$-$\varepsilon$ Realizable and $k$-$\varepsilon$ RNG turbulence models, which are within about 4% of the experimental value, are almost as accurate. The standard $k$-$\omega$ model, however, gives a significant over prediction of the normal force coefficient, totally unacceptable for any engineering application. For the axial force coefficient, $C_A$, which is the most sensitive to the accurate prediction of the boundary layers, the closest predictions to the experimental value were found to be from the Baldwin-Lomax / Degani-Schiff model, the $k$-$\omega$ SST model and from Solution Adaptive Simulation all of which, remarkably, provided predictions to within 2% of the measured value. Both the Spalart-Allmaras and the $k$-$\varepsilon$ Realizable result were within 3-4% of the measured value. Interestingly neither the Reynolds Stress Model nor Detached Eddy Simulation provided as accurate predictions of these forces as the above mentioned methods, which is somewhat counter intuitive and needs some investigation. The standard $k$-$\omega$ model, again, compared poorly with all the other methods, giving a ~20% overprediction in $C_A$.

The pitching moment coefficient, $C_M$, about the nose ($x/D = 0$), is a function of the distribution of force along the body and so is highly sensitive to the evolution of the vortices along the body, and their associated leeside suctions. For this parameter all of the turbulence method underpredicted the experimentally measured value except for the standard $k$-$\omega$ model, which overpredicted $C_M$ by over 20%. The closest predictions were provided by the Baldwin-Lomax / Degani-Schiff and the $k$-$\varepsilon$ RNG turbulence models and the Solution Adaptive Simulation method, which gave $C_M$ to within 3% of the experimentally measured value. The result from the $k$-$\omega$ SST and $k$-$\varepsilon$ Realizable models were also very close, to within 5% of the measured value. For the accurate resolution of the axial centre of pressure the $k$-$\omega$ SST model gave by far the closest prediction to the experimental value, being within 0.2% of the measured value. The standard $k$-$\varepsilon$ and $k$-$\varepsilon$ Realizable models and Solution Adaptive

Simulation provided results that were within 1% of the experimental figure. Given that the experimental accuracy could probably be quoted to be within 2% of the quoted figure, all four of these turbulence models could be regarded as equally accurate. The standard $k\text{-}\omega$ model gave a consistently poor prediction – overpredicting $C_M$ by over 20%.

Overall for this test case the Solution Adaptive Simulation method appears to have most consistently predicted the overall flow structure of the leeside primary vortex and its associated embedded shock wave, together with the most accurate predictions of the surface pressure distribution along the body and the corresponding overall forces and moments. Of the RANS turbulence models, the $k\text{-}\varepsilon$ Realizable and $k\text{-}\omega$ SST models provided the most accurate results, but were not as consistently accurate as Solution Adaptive Simulation.
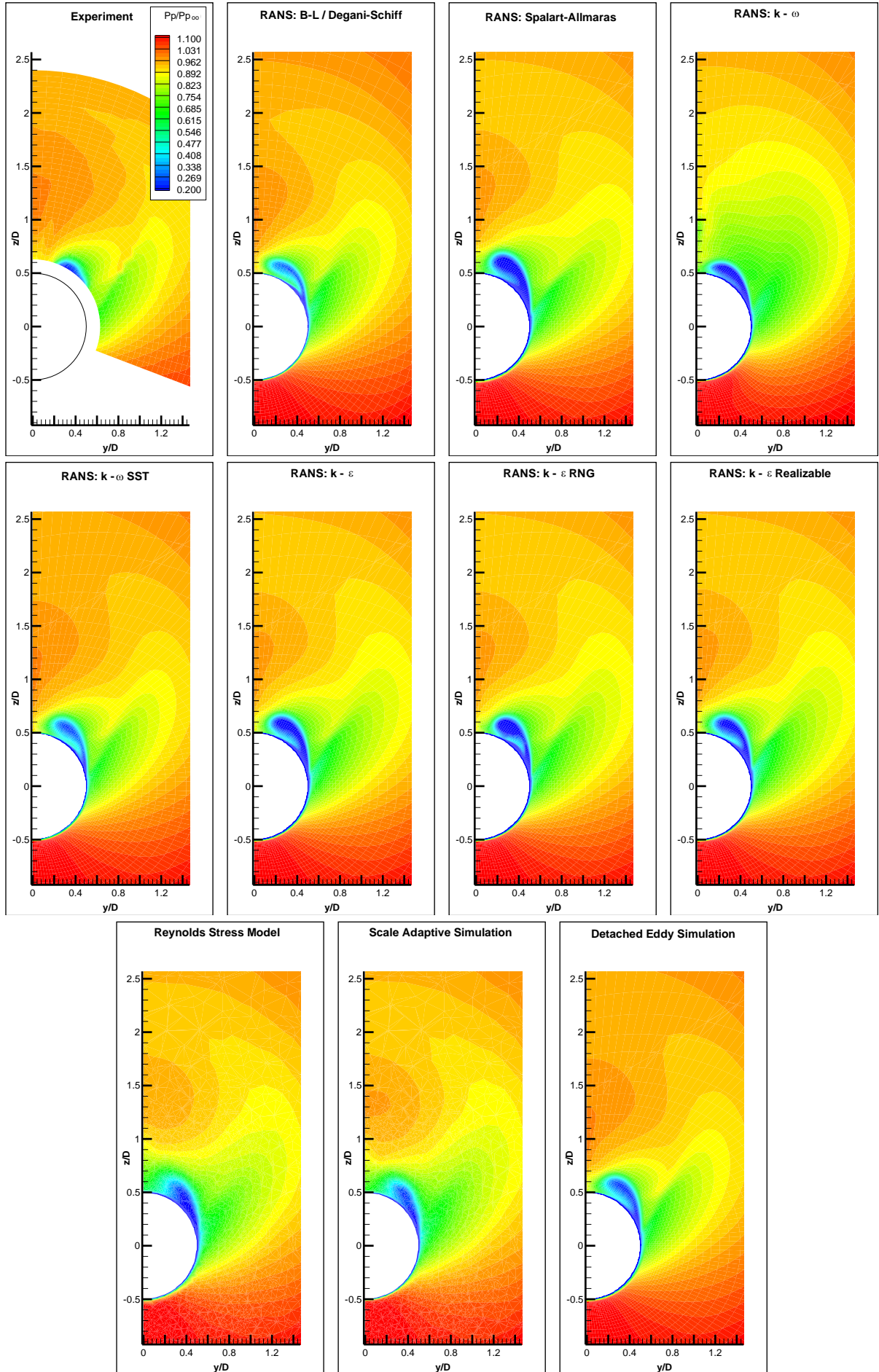
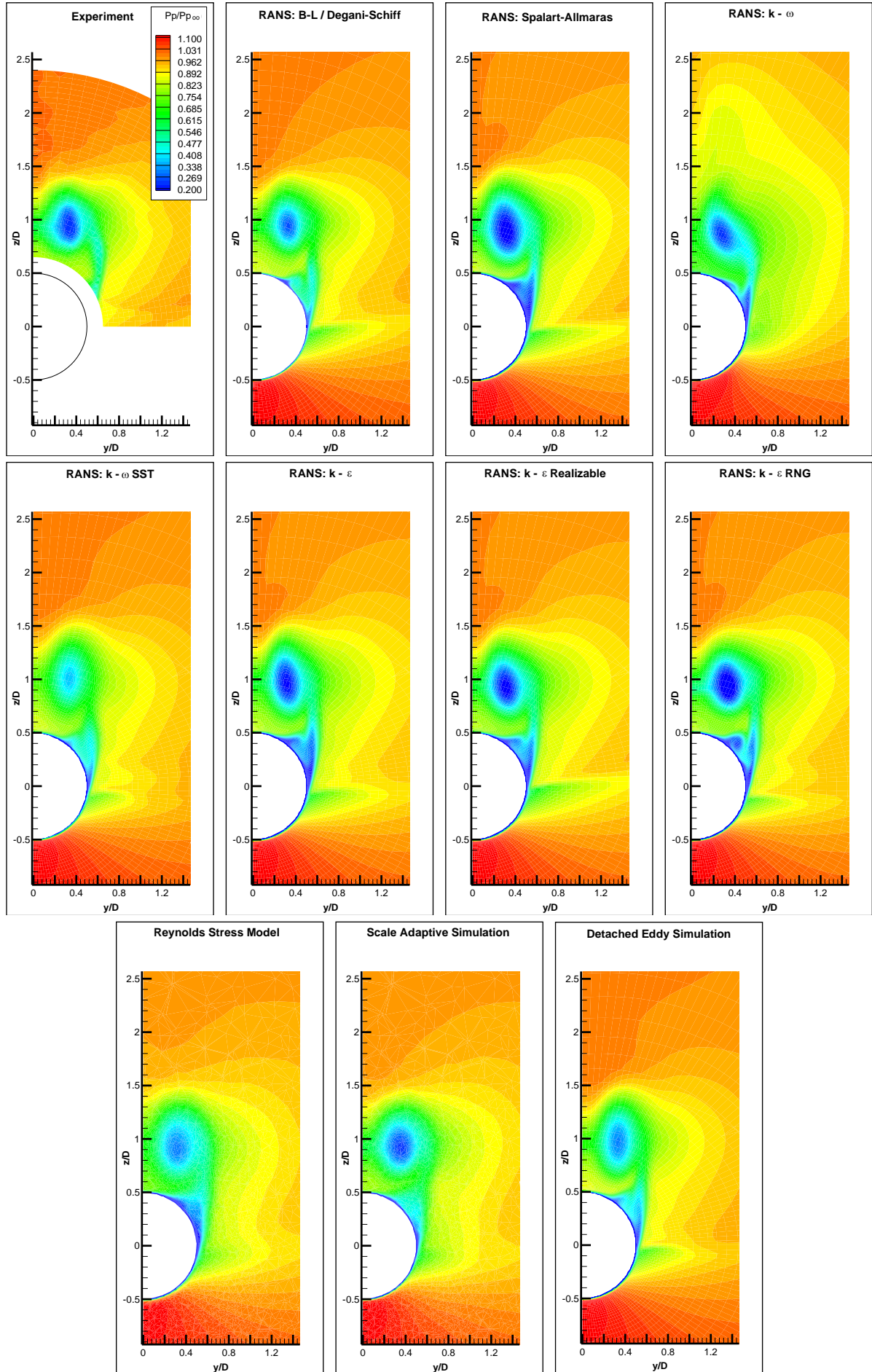*Figure 24: Comparison of total pressure ratio, B1A, α = 14°, M=2.50, Re$_D$=1.123x10$^6$, x/D=5.5*

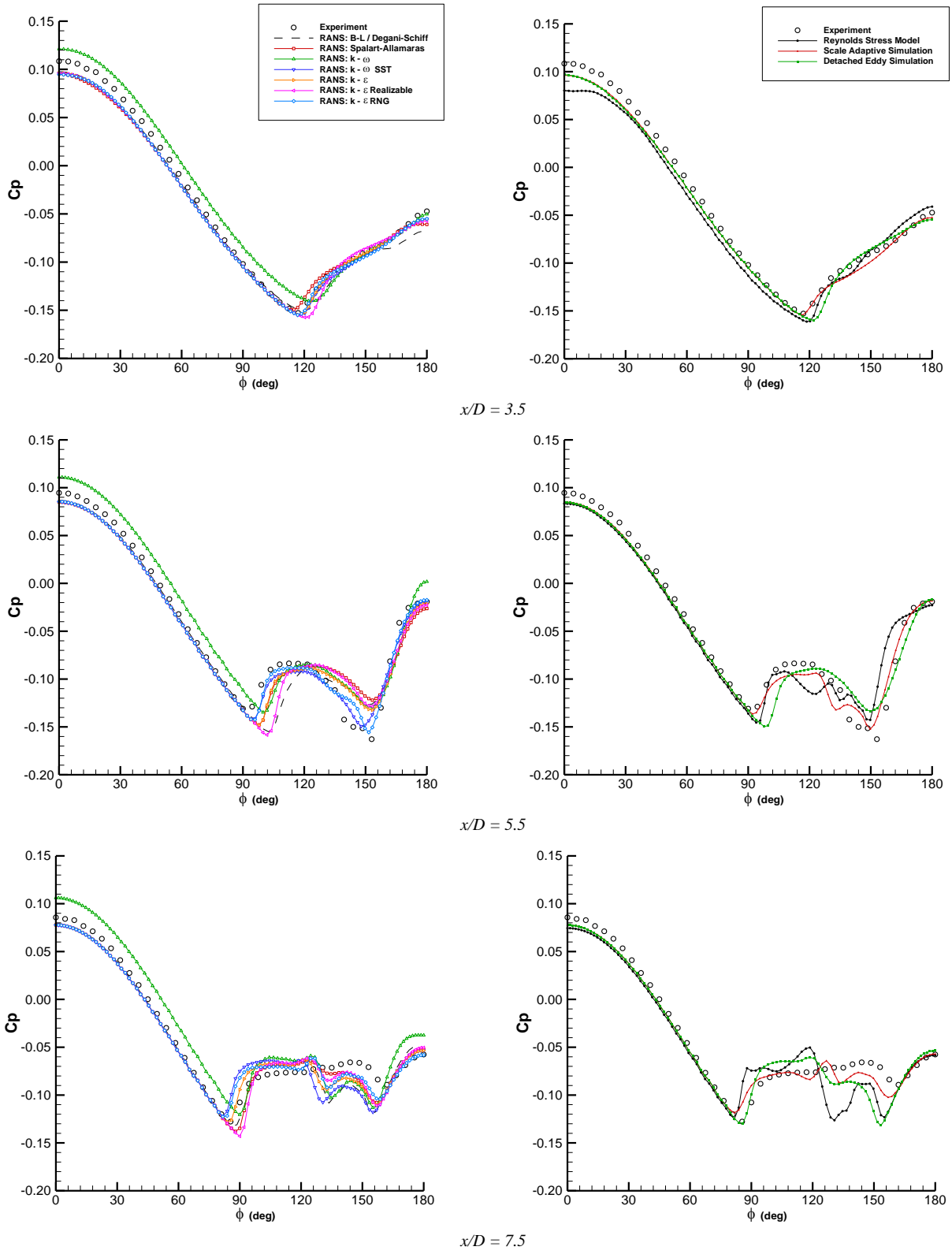*Figure 25: Comparison of total pressure ratio, B1A, $\alpha = 14^o$, M=2.50, $Re_D=1.123x10^6$, x/D=11.5*

*Figure 26: Comparison of circumferential surface Cp distribution, B1A, α = 14º, M=2.50, Re_D=1.123x10⁶. RANS predictions (left), and scale resolving predictions (right).*
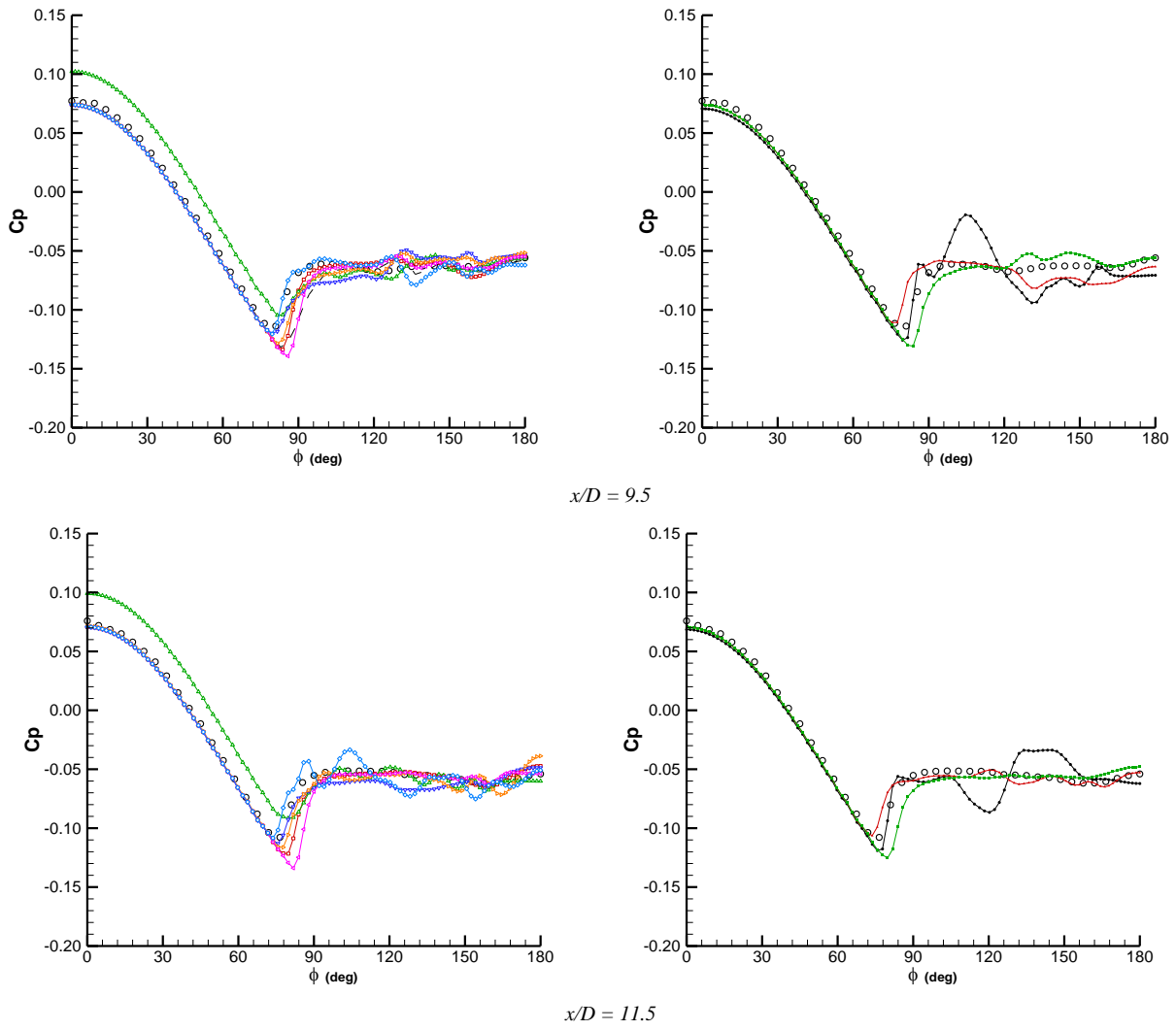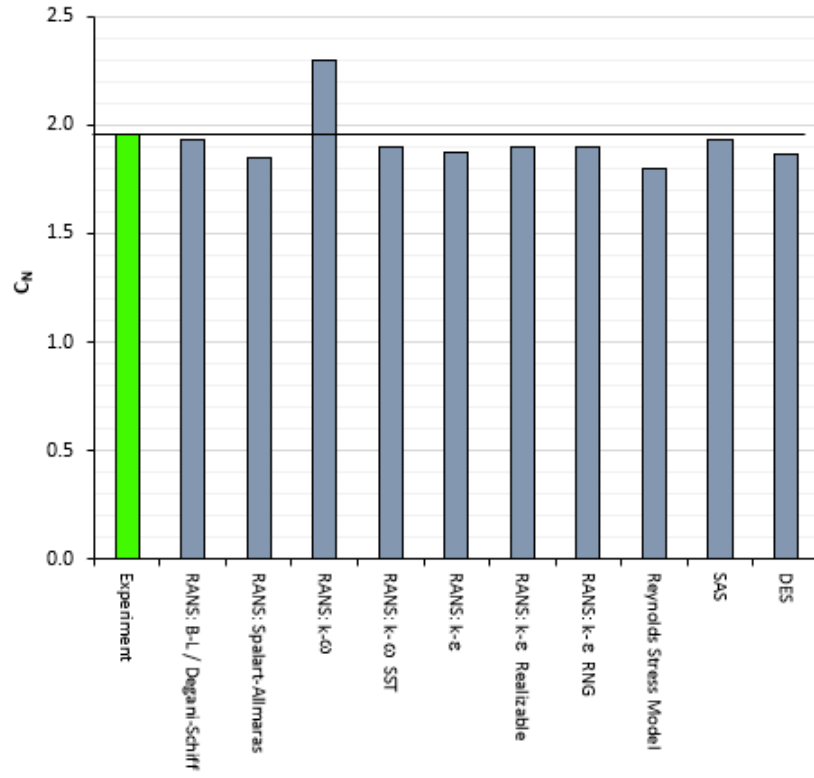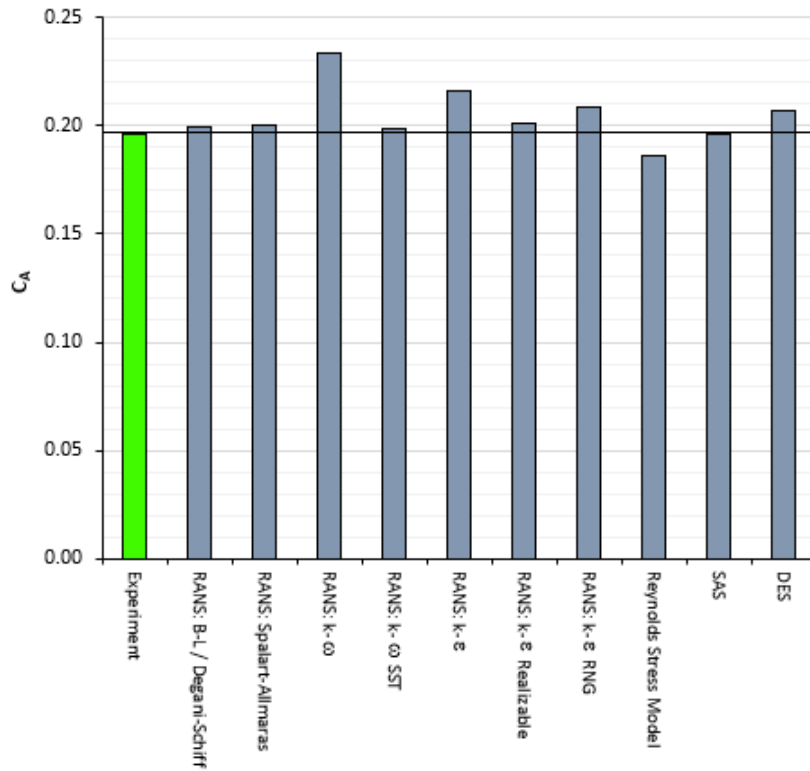
50

*x/D = 9.5*



*x/D = 11.5*

*Figure 26: Comparison of circumferential surface Cp distribution, B1A, α = 14º, M=2.50, Re_D=1.123x10^6 (concluded). RANS predictions (left), and scale resolving predictions (right).*
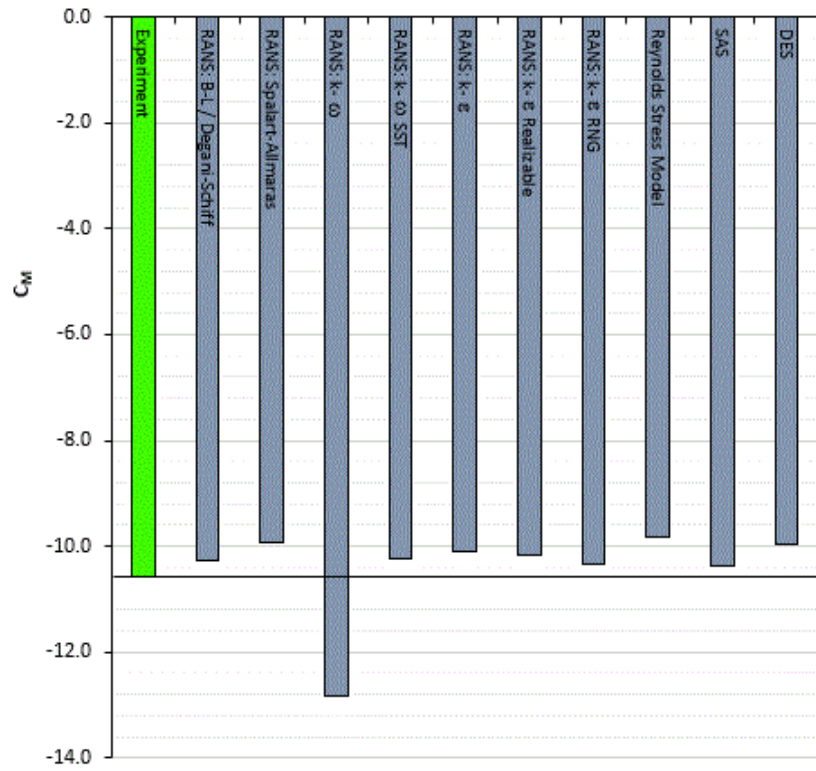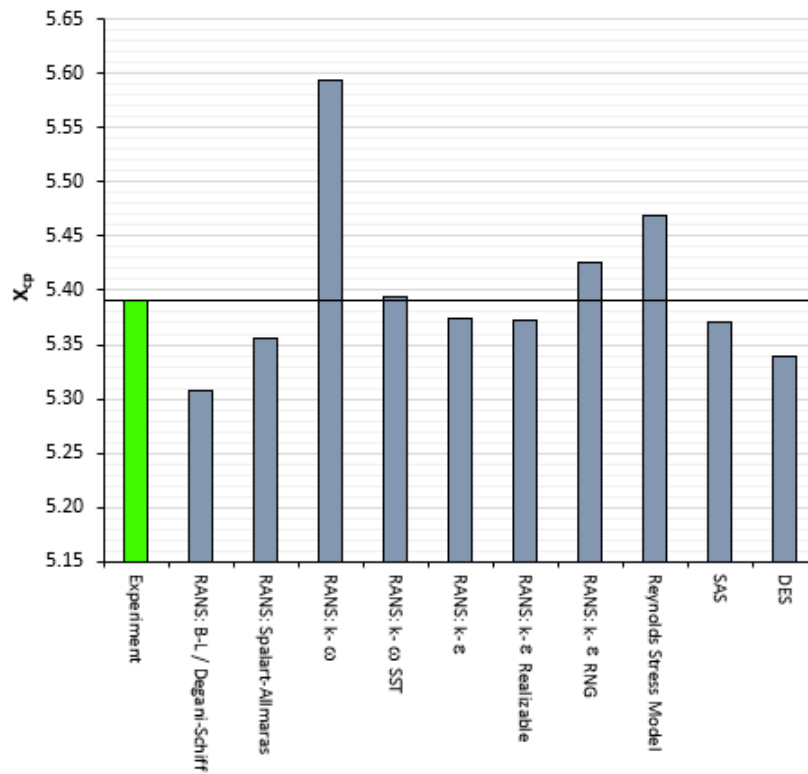
*a) Normal force coefficient, $C_N$.*



*b) Axial force coefficient, $C_A$.*

*Figure 27: Comparison of measured and predicted force and moment characteristics, B1A, $\alpha = 14^o$, M=2.50, $Re_D=1.123x10^6$.*

*c)  Pitching moment about the nose, $C_M$.*



*d)  Centre of pressure location from the nose, $x_{cp}$.*

*Figure 27: Comparison of measured and predicted force and moment characteristics, B1A, $\alpha = 14^o$, M=2.50, $Re_D=1.123x10^6$(concluded).*

# 5. Conclusions

The systematic comparison of the main modern turbulence prediction methods for the solution of the Navier-Stokes equations for the calculation of high speed flows about slender forebodies at low to moderate angle of attack, and where smooth surface turbulent boundary layer separation results in steady symmetric leeside vortices, has shown that:

- The method which most consistently provides accurate predictions of the overall forces and moments on the body, the most accurate distribution of surface pressure and can most accurately resolve the flow features, including leeside vortices and embedded shock wave features, is the Solution Adaptive Simulation method.

- Detached Eddy Simulation and the Reynold Stress Model, which would be expected to provide superior accuracy over the RANS based linear eddy viscosity models, on the whole failed to provide better predictions. In fact, the $k$-$\varepsilon$ Realizable turbulence model and the $k$-$\omega$ SST turbulence model provided data which was almost as consistently accurate as the Solution Adaptive Simulation method.

- The standard $k$-$\omega$ turbulence model appears to be completely unsuitable for the computation of this class of high speed flow problem, and this may be associated with the poor initial / default prescription of the value of $\omega$ at the far-field boundary. A separate systematic study of this turbulence model for this application is recommended to provide a definitive answer to this question. The $k$-$\varepsilon$ model is also seen to be too dissipative for the accurate resolution of the leeside vortices in this class of flow.

# References

[1] Esch H., "Bodies". AGARD Lecture Series-98., (Missile Aerodynamics), 1979.

[2] Wardlaw A. B. High Angle of Attack Missile Aerodynamics. AGARD Lecture Series-98., (Missile Aerodynamics), 1979.

[3] Deniau H., Lafon A. and Moschetta J. M. Progress in the Development And Validation of Turbulence Models for the Computation of Supersonic Flows With Crossflow Separation. AIAA Paper 95-0090,1995.

[4] d'Espiney, P., Champigny, P., Baudin, D., and Pilon, J. A. "Couch limite autour d'un fuselagede missile en incidence en ecoulement supersonique Etude experimentale et calcus Navier Stokes" Paper 19, AGARD AR-345, April 1998.

[5] Barberis, D. "Supersonic Vortex Flow Around A Missile Forebody", Test Case C5 in "A Selection of Experimental Test Cases for the Validation of CFD Codes, Volume 1", AGARD AG-303, August 1994.

[6] Ward, L. C. Pressure Measurements on an Axisymmetric Body at Mach Numbers from 2.5 to 4.5 RAE TM Aero 2174,1990.

[7] Ward, L. C. and Birch, T. J. An Investigation of Reynolds Number Effects on a Tangent-Ogive Cylinder Body. DRA TM Aero/Prop 4, May 1992.

[8] Hodges, J., Ward, L. C. and Birch, T. J. Pressure Measurements on Slender Bodies at Supersonic Speeds and Developments of Flow Separation Criteria for Euler Codes. RAE TM Aero 2177,1990.

[9] H. K. Versteeg and W. Malalasekera, An Introduction to Computational Fluid Dynamics, 2nd ed. Pearson Education, 2007.

[10] S. A. Prince, "The aerodynamics of high speed aerial weapons", Cranfield University, PhD thesis, 1999

[11] J. M. Luckring, "The discovery and prediction of vortex flow aerodynamics", The Aeronautical Journal, Vol. 123 No. 1264, pp 729-804, April 2019

[12] P. Moin and K. Mahesh," Direct numerical simulation: A tool in turbulence research", Center for Turbulence Research, Stanford University, Annual Review of Fluid Mechanics, vol. 30:539–78, 1998

[13] D. McLean, "Understanding Aerodynamics, arguing from the real physics". Wiley, 2013.

[14] T. Nishino, G. T. Roberts, and X. Zhang, "Unsteady RANS and detached-eddy simulations of flow around a circular cylinder in ground effect", J. Fluids Struct., vol. 24, no. 1, pp. 18–33, 2008.

[15] L. Davidson, "Fluid mechanics, turbulent flow and turbulence modeling", CFD course, Division of fluid Dynamics, Chalmers University of Technology. Division of fluid dynamics, Chalmers University of Technology, pp. 1–270, 2020.

[16] P. R. Spalart, S. Deck, M. L. Shur, K. D. Squires, M. K. Strelets, and A. Travin, "A new version of detached-eddy simulation, resistant to ambiguous grid densities", Theor. Comput. Fluid Dyn., vol. 20, no. 3, pp. 181–195, 2006.

[17] F. R. Menter and Y. Egorov, "The scale-adaptive simulation method for unsteady turbulent flow predictions. part 1: Theory and model description", vol. 85, no. 1, pp. 113–138, 2010.

[18] F. R. Menter, M. Kuntz, and R. Bender, "A Scale-Adaptive Simulation Model for Turbulent Flow Predictions", AIAA 2003-0767, 41st Aerospace Sciences Meeting and Exhibit, 2003, no. January.

[19] "ANSYS Fluent Theory Guide", no. 15, ANSYS Inc., USA, 2013.

[20] Baldwin, B. S. and Lomax, H., "Thin Layer Approximation and Algebraic Model for Separated Turbulent Flows", AIAA Paper 78-257, 1978.

[21] Cebici T. and Smith A. M. O. "Analysis of Turbulent Boundary Layers", Ser. in Appl. Math. and Mech., Vol. XV, Academic Press 1974

[22] Degani, D. and Schiff, L. B. "Computation of turbulent supersonic flows around pointed bodies having crossflow separation", Journal of Computational Physics, Volume 66, Issue 1, September 1986, Pages 173-196.

[23] Spalart, P. R. and Allmaras, S. R., "A One-Equation Turbulence Model for Aerodynamic Flows", AIAA Paper 92-0439, 1992.

[24] Bredberg, J., "On Two-equation Eddy-Viscosity Models", Chalmers University of Technology, Department of Thermo and Fluid Dynamics, Sweden, 2001.

[25] Asproulias, I., "RANS Modelling for Compressible Turbulent Flows Involving Shock Wave Boundary Layer Interactions", University of Manchester, 2014.

[26] Wilcox D. C., "Turbulence modeling for CFD", DCW Indistries, 3rd ed. 2006.

[27] Launder, B.E.; Spalding, D.B., "The numerical computation of turbulent flows", Computer Methods in Applied Mechanics and Engineering. 3 (2): 269–289., 1974.

[28] Jones, W. P., and Launder, B. E., "The Prediction of Laminarization with a Two-Equation Model of Turbulence", International Journal of Heat and Mass Transfer, vol. 15, pp. 301-314., 1972.

[29] Launder, B. E., and Sharma, B. I., "Application of the Energy Dissipation Model of Turbulence to the Calculation of Flow Near a Spinning Disc", Letters in Heat and Mass Transfer, vol. 1, no. 2, pp. 131-138, 1974.

[30] T.-H. Shih, W. W. Liou, A. Shabbir, Z. Yang, and J. Zhu. "A New k- epsilon Eddy-Viscosity Model for High Reynolds Number Turbulent Flows - Model Development and Validation" Computers Fluids, 24(3):227-238, 1995.

[31] Menter F. R., "Zonal Two Equation k-ω Turbulence Models for Aerodynamic Flows", AIAA Paper 93-2906., 1993.

[32] Yakhot V., Orszag S.A., Thangam S., Gatski T.B. & Speziale C.G., "Development of turbulence models for shear flows by a double expansion technique", Physics of Fluids A, Vol. 4, No. 7, pp1510-1520., 1992.

[33] Speziale C. G. and Thangam S., "Analysis of an RNG based turbulence model for separated flows", NASA CR 189600, 1992.

[34] Wilcox D.C., "Re-assessment of the scale-determining equation for advanced turbulence models", AIAA Journal, vol. 26, no. 11, pp. 1299-1310, 1988.

[35] Wilcox D. C., "Comparison of Two-equation Turbulence Models for Boundary Layers with Pressure Gradients", AIAA J., Vol. 31, No. 8, pp. 1414– 1421,1993.

[36] Menter F. R., "Performance of Popular Turbulence Models for Attached and Separated Adverse Pressure Gradient Flow", AIAA J., Vol. 30, pp. 2066–2072,1992

[37] Wilcox  D. C., "Simulation of transition with a two-equation turbulence Model", AIAA J., Vol. 32, pp. 247–255,1994.

[38] Menter F. R., "Two-Equation Eddy-Viscosity Turbulence Models for Engineering Applications", AIAA Journal, vol. 32, no 8. pp. 1598-1605., 1994.

[39] Menter F. R., Kuntz, M. and Langtry, R., "Ten Years of Industrial Experience with the SST Turbulence Model", Proceedings of the Fourth International Symposium on Turbulence, Heat and Mass Transfer, Begell House, Redding, CT, 2003.

[40] B. E. Launder, "Second-moment closure and its use in modelling turbulent industrial flows", Int. J. Numer. Methods Fluids, vol. 9, no. 8, pp. 963–985, 1989, doi: 10.1002/fld.1650090806.

[41] Launder B. E., Reece G. J. and Rodi W., "Progress in the Development of a Reynolds-Stress Turbulent Closure", Journal of Fluid Mechanics, Vol. 68(3), pp. 537-566., 1975.